

Genetic architecture and evolution of color variation in American black bears

Highlights

- The cinnamon morph of American black bears is due to a missense mutation in *TYRP1*
- Bear *TYRP1* variants are hypomorphs that impair protein localization to melanosomes
- The cinnamon variant arose 9,360 years ago and provides an adaptive advantage

Authors

Emily E. Puckett, Isis S. Davis,
Dawn C. Harper, ...,
Christopher B. Kaelin,
Michael S. Marks, Gregory S. Barsh

Correspondence

emily.puckett@memphis.edu

In brief

Puckett et al. show that a single base-paired variant in *TYRP1* results in the iconic cinnamon morph of the American black bear. They demonstrate that *TYRP1* variants in black and grizzly bears are loss-of-function alleles and impair protein localization to melanosomes. The black bear allele arose 1,440 generations ago in the southwestern range.



Article

Genetic architecture and evolution of color variation in American black bears

Emily E. Puckett,^{1,30,31,*} Isis S. Davis,^{1,26} Dawn C. Harper,² Kazumasa Wakamatsu,³ Gopal Battu,⁴ Jerrold L. Belant,⁵ Dean E. Beyer, Jr.,⁵ Colin Carpenter,⁶ Anthony P. Crupi,⁷ Maria Davidson,^{8,27} Christopher S. DePerno,⁹ Nicholas Forman,¹⁰ Nicholas L. Fowler,⁷ David L. Garshelis,^{11,12} Nicholas Gould,⁹ Kerry Gunther,¹³ Mark Haroldson,¹⁴ Shosuke Ito,³ David Kocka,¹⁵ Carl Lackey,¹⁶ Ryan Leahy,^{17,28} Caitlin Lee-Roney,¹⁷ Tania Lewis,¹⁸ Ashley Lutto,¹⁹

(Author list continued on next page)

¹Department of Biological Sciences, University of Memphis, Memphis, TN 38152, USA

²Department of Pathology and Laboratory Medicine, Children's Hospital of Philadelphia, Philadelphia, PA 19104, USA

³Institute for Melanin Chemistry, Fujita Health University, Toyoake, Japan

⁴HudsonAlpha Institute for Biotechnology, Huntsville, AL 35806, USA

⁵Department of Fisheries and Wildlife, Michigan State University, East Lansing, MI 48824, USA

⁶West Virginia Division of Natural Resources, Beckley, WV 25801, USA

⁷Division of Wildlife Conservation, Alaska Department of Fish and Game, Douglas, Juneau, AK 99824, USA

⁸The Louisiana Department of Wildlife and Fisheries, Baton Rouge, LA 70898, USA

⁹Department of Forestry and Environmental Resources, North Carolina State University, Raleigh, NC 27695-7646, USA

¹⁰New Mexico Department of Game and Fish, Santa Fe, NM 87507, USA

¹¹Minnesota Department of Natural Resources, Grand Rapids, MN 55744, USA

¹²IUCN SSC Bear Specialist Group

¹³National Park Service, Yellowstone National Park, WY 82190-0168, USA

¹⁴U.S. Geological Survey, Northern Rocky Mountain Science Center, Interagency Grizzly Bear Study Team, Bozeman, MT 59715, USA

¹⁵Virginia Department of Wildlife Resources, Verona, VA 24482, USA

¹⁶Nevada Department of Wildlife, Reno, NV 89512, USA

¹⁷National Park Service, Yosemite National Park Wildlife Management, Yosemite, CA 95389, USA

(Affiliations continued on next page)

SUMMARY

Color variation is a frequent evolutionary substrate for camouflage in small mammals, but the underlying genetics and evolutionary forces that drive color variation in natural populations of large mammals are mostly unexplained. The American black bear, *Ursus americanus* (*U. americanus*), exhibits a range of colors including the cinnamon morph, which has a similar color to the brown bear, *U. arctos*, and is found at high frequency in the American southwest. Reflectance and chemical melanin measurements showed little distinction between *U. arctos* and cinnamon *U. americanus* individuals. We used a genome-wide association for hair color as a quantitative trait in 151 *U. americanus* individuals and identified a single major locus ($p < 10^{-13}$). Additional genomic and functional studies identified a missense alteration (R153C) in *Tyrosinase-related protein 1* (*TYRP1*) that likely affects binding of the zinc cofactor, impairs protein localization, and results in decreased pigment production. Population genetic analyses and demographic modeling indicated that the R153C variant arose 9.36 kya in a southwestern population where it likely provided a selective advantage, spreading both northwards and eastwards by gene flow. A different *TYRP1* allele, R114C, contributes to the characteristic brown color of *U. arctos* but is not fixed across the range.

INTRODUCTION

Variation in animal color is a long-standing system with which to investigate gene action and evolution. In mammals, nearly all pigment is produced by melanocytes via polymerization of dihydroxyindole derivatives to yield insoluble melanins that are transferred to overlying keratinocytes in skin and/or hair. Genetic variation in melanin biosynthesis or transfer gives rise to hair, eye, and skin color differences and can underlie positive

selection.^{1,2} Mutations of melanin biosynthesis underlie a number of conditions associated with impaired fitness or a disease (e.g., human albinism), or unusual color morphs of large mammals that are specifically targeted for trophy hunting.³

Identifying and understanding the genetic causes and consequences of mammalian color variation is of special interest in large mammals for two reasons. First, by contrast to small mammals in which color morphs are often selected as a means of predator avoidance, the evolutionary forces underlying color



Kelly McGowan,²⁰ Colleen Olfenbittel,²¹ Mike Orlando,²² Alexander Platt,²³ Matthew D. Pollard,¹ Megan Ramaker,^{4,29} Heather Reich,¹⁶ Jaime L. Sajecki,¹⁵ Stephanie K. Sell,⁷ Jennifer Strules,⁹ Seth Thompson,¹⁵ Frank van Manen,¹⁴ Craig Whitman,¹⁴ Ryan Williamson,²⁴ Frederic Winslow,¹⁰ Christopher B. Kaelin,²⁰ Michael S. Marks,^{2,25} and Gregory S. Barsh^{4,20}

¹⁸National Park Service, Glacier Bay National Park, Gustavus, AK 99826, USA

¹⁹U.S. Fish and Wildlife Service, Kenai National Wildlife Refuge, Soldotna, AK 99669, USA

²⁰Department of Genetics, School of Medicine, Stanford University, Stanford, CA 94305, USA

²¹North Carolina Wildlife Resources Commission, Raleigh, NC 27699, USA

²²Florida Fish and Wildlife Conservation Commission, Tallahassee, FL 32399, USA

²³Department of Genetics, Perelman School of Medicine, University of Pennsylvania, Philadelphia, PA 19104, USA

²⁴National Park Service, Great Smoky Mountains National Park, Gatlinburg, TN 37738, USA

²⁵Departments of Pathology and Laboratory Medicine and of Physiology, Perelman School of Medicine, University of Pennsylvania, Philadelphia, PA 19104, USA

²⁶Present address: Ecology and Evolutionary Biology, Texas A&M University, College Station, TX 77843-2475, USA

²⁷Present address: Safari Club International Foundation, Tucson, AZ 85745, USA

²⁸Present address: Wildlife Branch, California Department of Fish and Wildlife, Rancho Cordova, CA 95670, USA

²⁹Present address: Duke Molecular Physiology Institute, Duke University School of Medicine, Durham, NC 27701, USA

³⁰Twitter: @EEPuckett

³¹Lead contact

*Correspondence: emily.puckett@memphis.edu

<https://doi.org/10.1016/j.cub.2022.11.042>

variation in large mammals are less apparent. Second, there are often charismatic and/or cultural values associated with certain species and color morphs such as the black jaguar and white tiger. Despite their common name, American black bears, *Ursus americanus*, occur in black, cinnamon, brown, blond, gray, and white morphs; similarly, brown bears (*U. arctos*) occur in blond, brown, dark chocolate, white, and ruddy morphs. The cinnamon morph of *U. americanus* has a rich history in popular culture⁴ and systematics and has been suggested to have adaptive value, either by aiding in thermoregulation in hotter and drier climates of the southwest or by mimicry of *U. arctos* in areas where the two species are sympatric. Cinnamon has a distinct latitudinal gradient in western North America, with a high frequency in the southwest, which declines moving northward, and a low frequency in the east.⁵ This phenotypic variation is consistent with genomic analyses that indicate the deepest phylogeographic structuring occurring between the eastern and western lineages across North America.^{6,7} Further, admixture between the lineages has been identified across the northern range and suggested to be a product of post-glacial range expansion and east-west gene flow across contiguous habitat in modern Canada.⁷

The distinct spatial distribution of cinnamon *U. americanus* presents three alternative phylogeographic hypotheses. First, the causative mutation arose in the western lineage after the split from the eastern lineage. Second, the variant predates lineage divergence but was lost during eastward range expansion. Third, introgression of the causative variant from *U. arctos* into *U. americanus* occurred in a western lineage population.

We used a genome-wide approach and identified the causative variant that produces cinnamon morphs in *U. americanus*, then applied molecular and population genetic approaches to explore its functional impact and demographic history. We identified a missense alteration in *Tyrosinase-related protein 1* (*TYRP1*) and showed that it interferes with melanin synthesis. We found the *U. americanus* *TYRP1* variant was not introgressed from *U. arctos*; instead, a different *TYRP1* variant contributes to their characteristic pigmentation phenotype. Remarkably, the

variant responsible for cinnamon *U. americanus* is identical to one previously described as a cause of oculocutaneous albinism (OCA3) in humans, often associated with nystagmus and reduced visual acuity.

Our analyses indicate that the cinnamon *TYRP1* variant arose within the western lineage of *U. americanus* and likely provided a selective advantage in the southwest. These results illustrate how Mendelian variation in melanogenesis can underlie iconic phenotypes and inform our understanding of color variation and recent evolution in large carnivores.

RESULTS AND DISCUSSION

Quantitative and chemical characterization of bear hair color

In addition to cinnamon, light-colored morphs of *U. americanus* have been described as blond, light brown, or chocolate; thus, the results presented reflect all of these color morphs. We measured reflectance of hair samples from 391 *U. americanus* and 33 *U. arctos* from across North America. Most *U. americanus* qualitatively described as black, based on photographs, exhibited reflectance values < 50 (median = 5), whereas animals scored as cinnamon had broadly ranging values (median = 67); overall, the distribution of reflectance varied continuously from 0.5 to 182 (possible range: 0–255; Figure 1A; Table S1). Reflectance in *U. arctos* also varied continuously (median = 48). Thus, we consider the reflectance measure a quantitative variable.

We determined if hair color of cinnamon *U. americanus* and *U. arctos* was caused by dilution of eumelanin or increased production of pheomelanin, using high-performance liquid chromatography (HPLC)^{8,9} of the different pigment types in awn hair samples. As depicted in Figures 1B and 1C, the major determinant of light-colored hair is reduced amounts of eumelanin in both bear species.

Allelic identification of TYRP1 variants

We sequenced the genomes of 24 *U. americanus* to $\geq 30\times$ depth and an additional 166 animals to $1.3\times$ depth, mapped to the

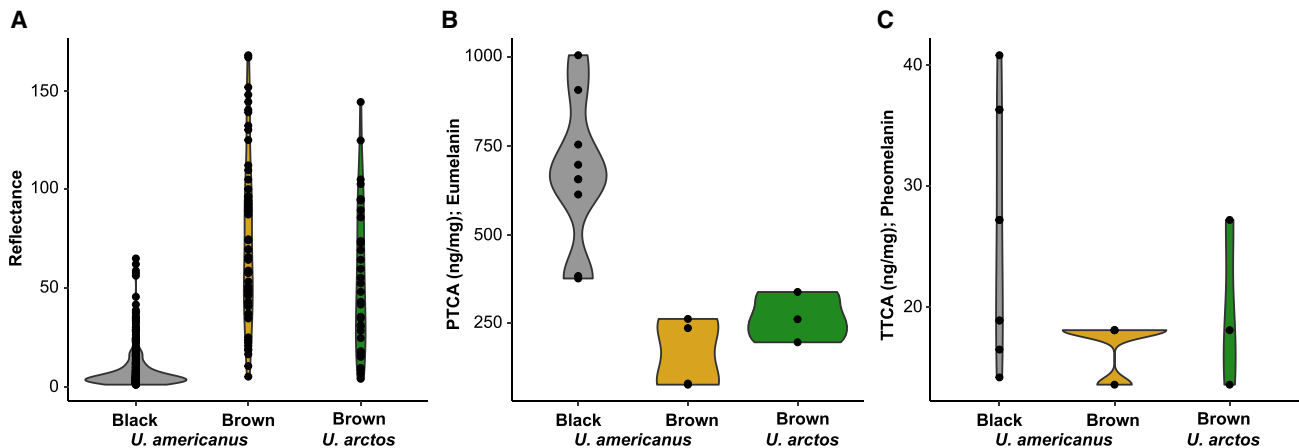


Figure 1. Characterization of bear hair color

(A) Violin plots of hair reflectance for two bear species (*Ursus americanus* [n = 327] and *U. arctos* [n = 33]) categorized by qualitative phenotyping from photos as either black or brown animals (black *U. americanus*, gray; brown *U. americanus*, yellow; brown *U. arctos*, green). Chemical analysis via alkaline hydrogen peroxide oxidation followed by high-performance liquid chromatography (HPLC) of 13 *U. americanus* and 3 *U. arctos* individuals' hair for the concentration of (B) eumelanin (as PTCA; ANOVA $F = 14.512$; $p < 0.001$) or (C) pheomelanin (as TTCA; ANOVA $F = 2.0297$; $p = 0.17$). PTCA concentration in hair ranged from 75 to 1,010 ng mg^{-1} , where TTCA was limited to 13–40 ng mg^{-1} in *U. americanus*. Specifically, two-tailed t tests between *U. americanus* black and brown animals ($p < 0.001$), and *U. americanus* black and *U. arctos*, were significantly different ($p < 0.001$), whereas no difference was observed between species with brown coloration ($p = 0.17$). In *U. arctos*, PTCA and TTCA ranged from 200 to 340 ng mg^{-1} and 13 to 27 ng mg^{-1} , respectively. Both species indicate a dilution of eumelanin, and not an increase in pheomelanin, produces the characteristic hair-lightening. See also Table S1.

reference genome,¹⁰ then imputed missing loci in the low-coverage samples using the high-coverage individuals as a reference panel.¹¹ A genome-wide association study (GWAS)¹² for quantitative hair reflectance values from 151 bears identified 120 single-nucleotide variants (SNVs) above a significance threshold of 10^{-8} (Figure 2A; Table S2). A single peak had the lowest p values and spanned the pigmentation gene *TYRP1* (Figure 2B), in which we identified a significant ($p = 1.99 \times 10^{-13}$) G to A SNV, HiC_scaffold_24:6724152g>a that predicts a missense alteration, p.Arg153Cys, referred to in what follows as *TYRP1*^{R153C}. This alteration within the luminal domain of TYRP1, a type I transmembrane protein, is within a critical region near the zinc cofactor binding site and thus is likely deleterious (Figure 2C). Nine additional SNVs had lower p values and were 130 kb downstream of the *TYRP1* transcription start site (Figure 2B); however, after accounting for *TYRP1*^{R153C} genotypes as a covariate, the significance of these sites fell below the genome-wide threshold. Further, haplotype analysis¹³ identified low diversity in the Nevada population, thus we used these samples as input into HAPLOVIEW¹⁴ and identified a single 97 kb haplotype carrying *TYRP1*^{R153C} (Figures 2B and S1). Recombination is apparent in populations outside of the southwest, suggesting that *TYRP1*^{R153C} is derived from a single mutational event.

We explored coding sequence variation in *TYRP1* and 12 additional pigmentation genes in *U. americanus*, *U. arctos*, and *U. maritimus* (polar bear). For *U. americanus*, we identified 46 missense or nonsense polymorphisms within 11 genes (Table S3); among these, only the *TYRP1*^{R153C} variant was correlated with color (Figure S2A) and predicted to be deleterious. We identified 19 missense variants between *U. americanus* and *U. arctos* and 33 missense or nonsense variants between

U. arctos and *U. maritimus* (Table S3). The *U. americanus* R153C variant was not observed in *U. arctos* or *U. maritimus*; however, a different *TYRP1* variant was identified in 60% of *U. arctos* individuals, HiC_scaffold_24:6725331g>a, that predicts a p.Arg114Cys substitution (*TYRP1*^{R114C}). Both mutations occur in the luminal domain of TYRP1, which contains 10 evolutionarily conserved cysteine (Cys) residues that form 5 disulfide bonds; acquisition of an unpaired Cys residue in *TYRP1*^{R153C} and *TYRP1*^{R114C} is likely to interfere with native disulfide bonding and protein folding (Table S3; Figures 2C and S2).¹⁵

We also examined *TYRP1* variation at orthologous positions in other species. In humans, loss of function for *TYRP1* causes a rare form of albinism, rufous OCA3, observed mostly in individuals of African or Puerto Rican ancestry and characterized by reddish skin and hair and frequent visual abnormalities.¹⁶ Among 15 individuals with clinical albinism and mutations of *TYRP1*, R114C and R153C were each observed once as compound heterozygotes.¹⁷ The R153C variant is found at a relatively high frequency in individuals of European ancestry, 7.91×10^{-4} , but is classified as a variant of uncertain significance.^{18,19} In laboratory rats, the R114C allele is likely responsible for a spontaneous brown mutation that is fixed in the Brown Norway strain.²⁰

Functional characterization

To test whether the *TYRP1* R153C and R114C variants affect function, we assessed their impact on pigmentation following expression in mouse melan-b cells, which are derived from *TYRP1*^{b/b} mutant mice and are hypopigmented due to the absence of functional or immunohistochemically detectable TYRP1. Wild-type (WT) mouse or human *TYRP1* can rescue pigmentation in melan-b cells. We introduced the *TYRP1* R153C or R114C variants into their orthologous positions in

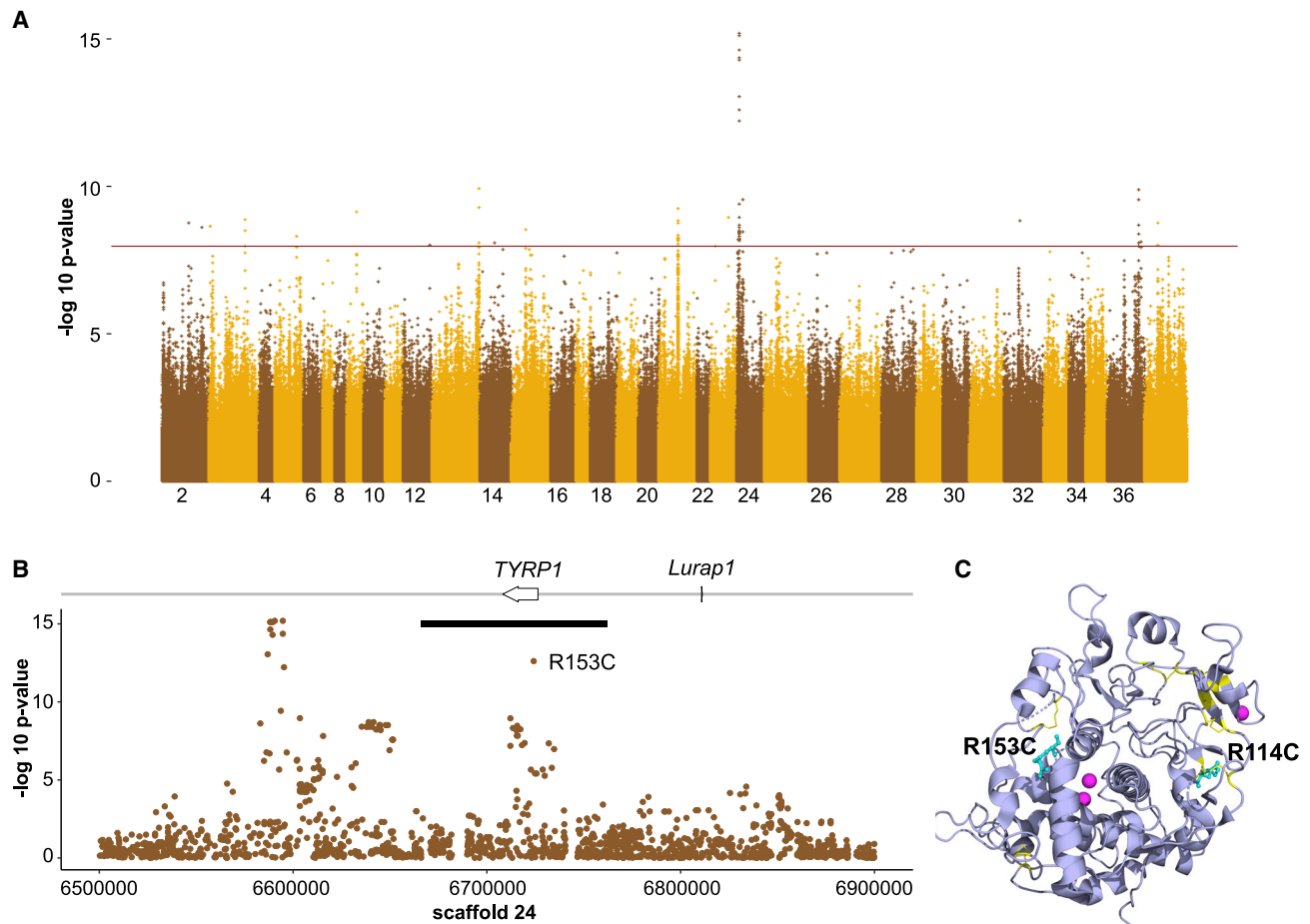


Figure 2. Genome-wide association study of American black bear coat color

GWAS of both high- and low-coverage WGS data from *Ursus americanus* ($n = 151$) to identify loci associated with coat color.

(A) A genome-wide Manhattan plot with a significance cutoff of 10^{-8} (horizontal brown line) identified a single strong peak on scaffold 24 (additional peaks in Table S2).

(B) A detailed view of scaffold 24 surrounding the peak identified two genes, including *TYRP1*. The black bar denotes the length of the haplotype identified within the Nevada population that contains the R153C-derived allele.

(C) The locations of R114 and R153 (cyan, shown in atomic format) are shown within a ribbon diagram of the 3D structure of the human *TYRP1* luminal domain (purple, from PDB: 5M8L¹⁵). Cys residues involved in disulfide bonds are yellow and the zinc cofactors are magenta. Note the proximity of R114 to a native disulfide bond and of R153 to a break between two alpha helices that are part of the zinc binding region.

See also Figure S2 and Table S2.

mouse and human *TYRP1* and expressed WT or variant *TYRP1*, or mCherry-syntaxin 13 (mCh-STX13) as a negative control, from recombinant retroviruses in melan-b cells. Using a colorimetric melanin content assay (Figure 3A), WT human *TYRP1* (h*TYRP1*) rescued pigmentation relative to control (untransfected or mCh-STX13-transfected) melan-b cells to nearly the same level as WT (melan-*Ink4a*) melanocytes. By contrast, the R153C and R114C variants rescued pigmentation in melan-b cells—respectively, only 52.0% and 14.1%, as well as WT h*TYRP1*, and 46.0% and 6.8%, as well as WT mouse *TYRP1*. This correlates with melanin quantification in bear hair detected by HPLC (Figure 1B), and it indicates that R153C and R114C are causal variants for reduced pigmentation.

To test if the defect in pigmentation reflected impaired localization of the variants to melanosomes, we examined melan-b cells transfected with the different constructs by bright-field

microscopy to visualize pigment granules and by immunofluorescence microscopy for *TYRP1*. The majority of melan-b cells transfected with WT h*TYRP1* are densely pigmented. By contrast, most cells expressing h*TYRP1*^{R153C} or h*TYRP1*^{R114C} were either non-pigmented or lightly pigmented; some of the latter contained large aggregates of pigment, perhaps reflecting melanosome autophagy (Figure 3B). By immunofluorescence microscopy, only background labeling for *TYRP1* was detected in melan-b cells that were untransduced (–; Figure 3G) or transduced with mCh-STX13 (Figure 3F). WT h*TYRP1* was detected predominantly in “rings” around pigment granules detected by bright-field microscopy (Figures 3C [arrowheads] and 3H), representing localization to the limiting membrane of mature melanosomes.²¹ By contrast, h*TYRP1*^{R114C} primarily localized to punctate and diffuse structures; the puncta did not overlap with pigment granules when present (Figures 3E

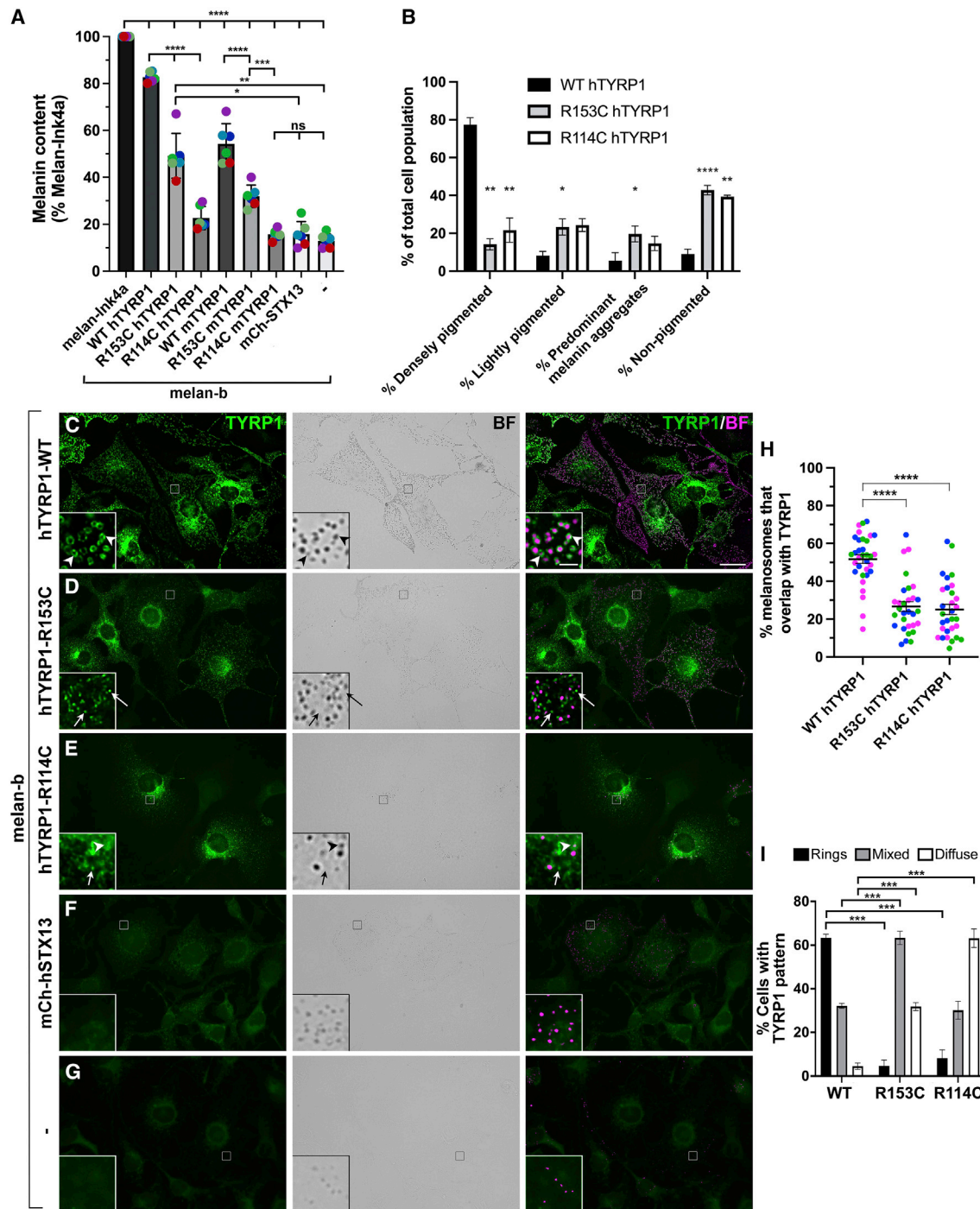


Figure 3. Functional characterization of TYRP1 alleles

(A) TYRP1-deficient melan-b cells that were untransduced (–) or stably expressing the WT, R153C, or R114C variants of human (h) or mouse (m) TYRP1 or mCh-STX13 as a control were analyzed by quantitative melanin content assay and normalized to protein content. Data represent percent normalized melanin content relative to that of WT melan-Ink4a cells from six experiments (colored dots), each performed in duplicate, and analyzed by two-way ANOVA and Tukey’s multiple comparison test.

(B) Stable melan-b transductants expressing WT, R153C, or R114C hTYRP1 variants were analyzed by bright-field microscopy, and individual cells were characterized as densely pigmented, lightly pigmented, light with dense aggregates, or non-pigmented. Data from three experiments with 200 of each cell type per experiment were analyzed by a mixed effect analysis with Tukey’s multiple comparison test relative to WT hTYRP1.

(C–G) Indicated untransduced (–; G) or stable melan-b transductants (C–F) were analyzed by immunofluorescence microscopy for TYRP1 (left, green) and bright-field microscopy (BF) for pigment granules (middle); right, overlay with pigment granules pseudocolored magenta. Insets, 7× magnification of boxed regions

(legend continued on next page)

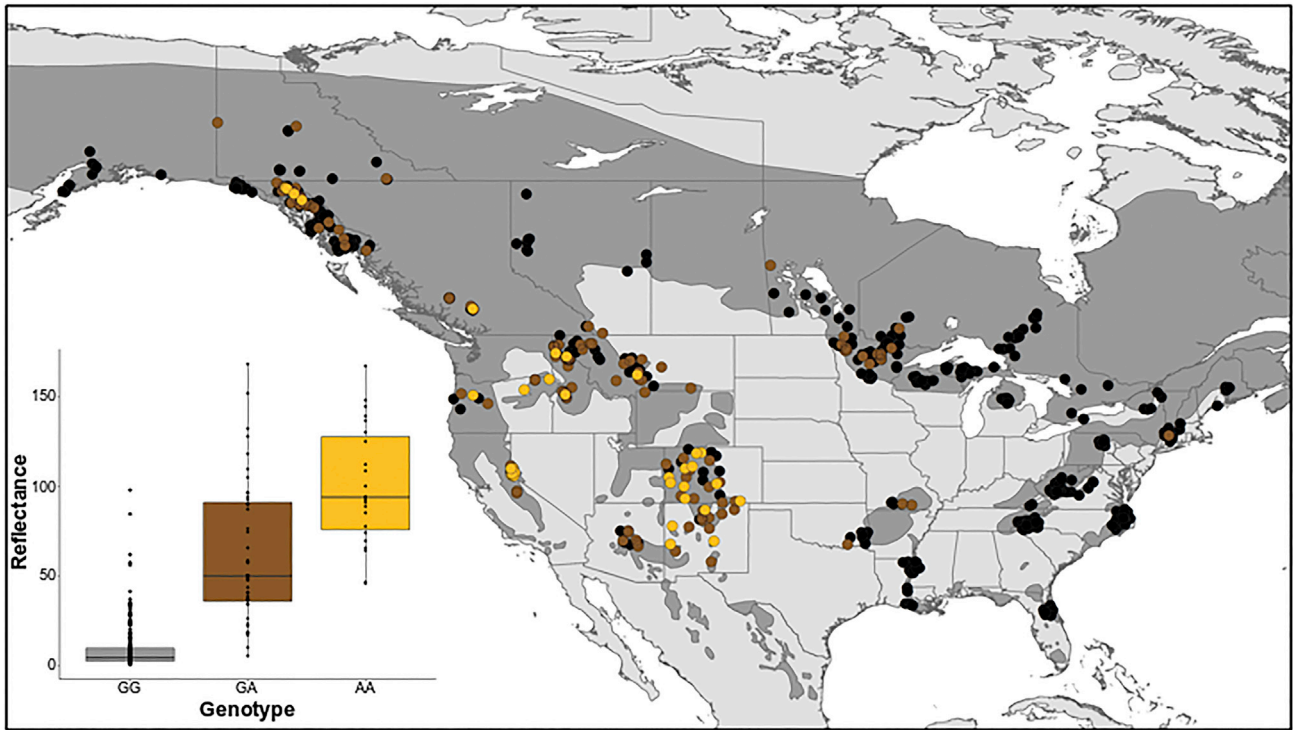


Figure 4. Spatial distribution of *TYRP1*^{R153C} across the American black bear range

Quantitative and spatial assessment of *TYRP1*^{R153C} in *Ursus americanus*. Inset: hair color reflectance was compared with the SNP genotype ($n = 317$). We used t tests to compare reflectance values between genotypes: homozygous ancestral and heterozygous, $p = 2.02 \times 10^{-11}$; heterozygous and homozygous derived, $p = 1.41 \times 10^{-4}$. These results indicate the allele acts with semidominance. The geospatial pattern of R153C across the range ($n = 906$) where color denotes genotype (black, homozygous ancestral GG; brown, heterozygous GA; gold, homozygous derived AA), with the species range shown in dark gray.

[arrows] and 3H). h*TYRP1*^{R153C} was mostly detected in a mixture of ring-like and diffuse/punctate patterns (Figures 3D and 3H). Since melanosome size and shape are determined prior to the onset of pigmentation,²² *TYRP1* would appear ring-like on both pigmented and non-pigmented melanosomes; thus, the reduced ring structures for h*TYRP1*^{R153C} and h*TYRP1*^{R114C} indicate that they do not localize properly to melanosomes. Considering only the cohort of cells that were densely pigmented, detectable pigment granules overlapped significantly less with *TYRP1* in cells expressing h*TYRP1*^{R153C} or h*TYRP1*^{R114C} than WT h*TYRP1* (Figure 3I). Given that the *TYRP1* luminal domain is required for proper melanosome localization,²³ we speculate that eumelanin dilution in bears may be explained by protein misfolding due to substitution of Cys for arginine (Arg) at residues 114 or 153, leading to enhanced protein degradation and impaired trafficking to and/or retention within melanosomes.

Gene action and spatial distribution of *TYRP1*^{R153C}

For *U. americanus*, examining hair reflectance as a function of *TYRP1*^{R153C} genotype in 317 individuals revealed semidominant gene action, with a median reflectance value for heterozygous G/A (Arg/Cys) individuals of 50.3 that was intermediate between values for homozygous G/G (Arg/Arg) and A/A (Cys/Cys) individuals of 4.7 and 94.0, respectively (Figure 4, inset).

We determined the spatial distribution of *TYRP1*^{R153C} in 906 samples across the species' geographic range. A high frequency of the derived allele was apparent in the southwest, declining northward along the Rocky Mountains into Southeast Alaska and Yukon Territory (Figure 4). By contrast, a low frequency of the derived allele was apparent in the eastern lineage, primarily limited to the Great Lakes region and a single sample in Connecticut, USA. The presence of the derived allele in Missouri, Arkansas, and Oklahoma, in the USA, was concordant with the known translocation history of bears from Minnesota

(intensities of *TYRP1* and pigment granules optimized to better visualize overlap). Arrowheads, *TYRP1* in rings around pigment granules; arrows, *TYRP1* in separate punctate structures.

(H) Quantification of cellular pattern of *TYRP1* as predominantly rings, diffuse/punctate, or mixed among transduced cells expressing each of the *TYRP1* variants. Data from four experiments with 150 of each cell type per experiment were analyzed by two-way ANOVA with Dunnett's multiple comparison test relative to WT *TYRP1*.

(I) Quantification of the percent of melanin-containing structures within densely pigmented cells that overlapped with *TYRP1*. Data from three experiments with 8–14 cells of each type (at least 30 in total) per experiment were analyzed by Kruskal-Wallis with Dunn's multiple comparison tests.

(A, B, H, and I) * $p < 0.05$; ** $p < 0.01$; *** $p < 0.001$; **** $p < 0.0001$.

See also Figure S2.

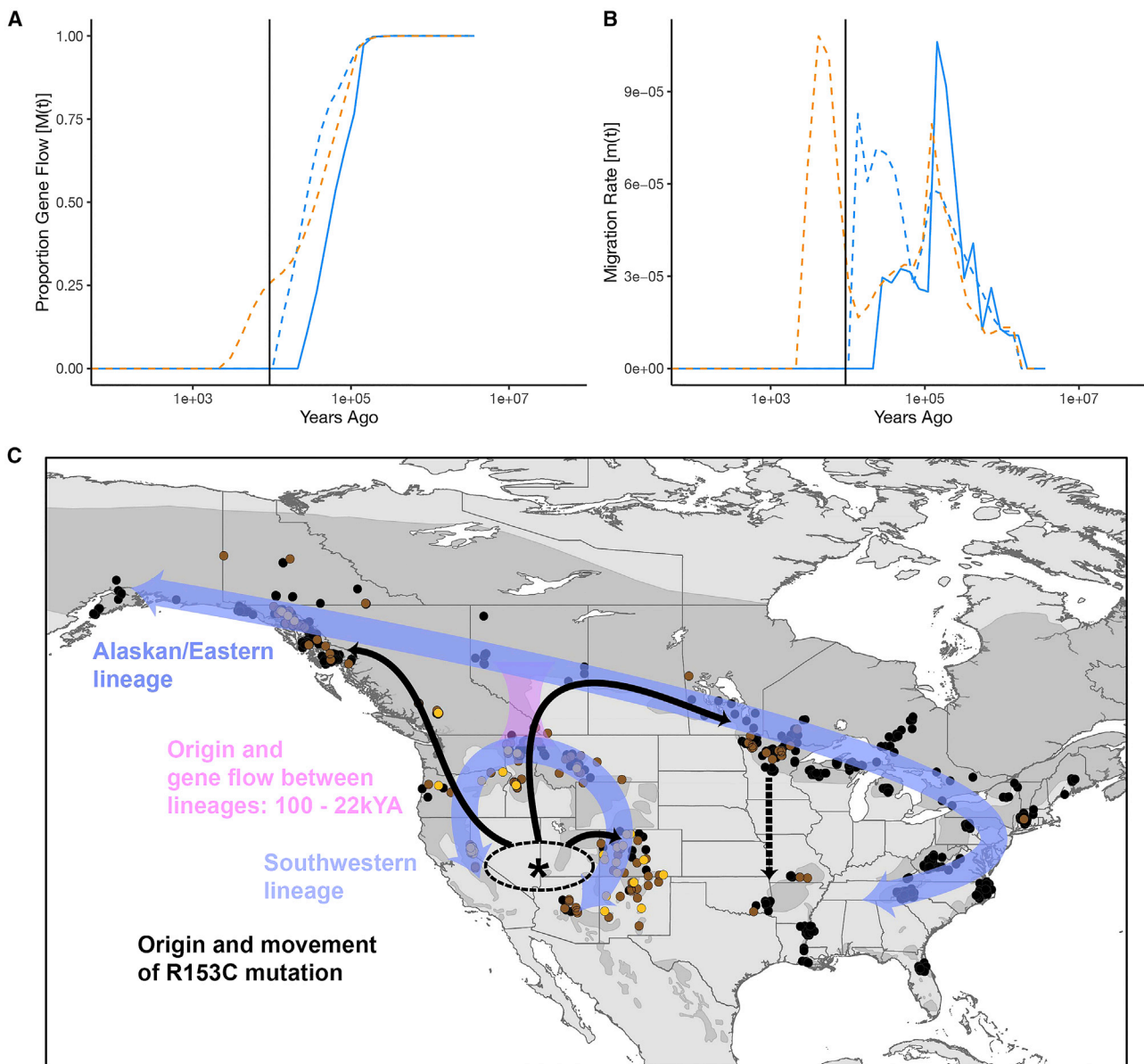


Figure 5. American black bear demographic history and $TYRP1^{R153C}$ allele expansion

(A and B) *Ursus americanus* demographic estimates over time. (A) Approximate completion of divergence and (B) bidirectional migration between lineage pairs, including eastern and western (solid blue line), eastern and Southeast Alaska (dashed blue line), and western and Southeast Alaska (dashed orange line). The vertical black line represents the estimated allele age of $TYRP1^{R153C}$ (see also Figure S3A).

(C) Our working model of historic lineage divergence (purple arrows), approximate geographic region of $TYRP1^{R153C}$ mutation (asterisks, *), and migration across the species' geographic range (solid black arrows; dashed black arrow indicating recent translocation).

See also Figure S3.

into Arkansas in the 1960s²⁴ and the high proportion of genetic diversity from the Great Lakes region now found in the Central Interior Highlands.²⁵ Spatial distribution of $TYRP1^{R153C}$ was consistent with the phenotypic distribution of non-black *U. americanus*, as estimated from a survey of 40,000 animals in the 1980s.⁵ Notably, $TYRP1^{R153C}$ was associated with bears qualitatively described as cinnamon, chocolate, or light brown, and it therefore accounts for the majority of color diversity among *U. americanus*.

Demography

Our $TYRP1$ haplotype tree (Figure S2A) indicated that introgression of *U. arctos* alleles into *U. americanus* did not provide the genetic material for light coloration in the latter species. We investigated the relationship of the $TYRP1^{R153C}$ mutation to *U. americanus* demographic history. First, we used *runtc*²⁶ to estimate the first coalescent (a proxy for allele age) of the variant along the scaffold and obtained a time of 9.36 kya. Second, we ran MSMC-IM²⁷ from whole-genome resequencing

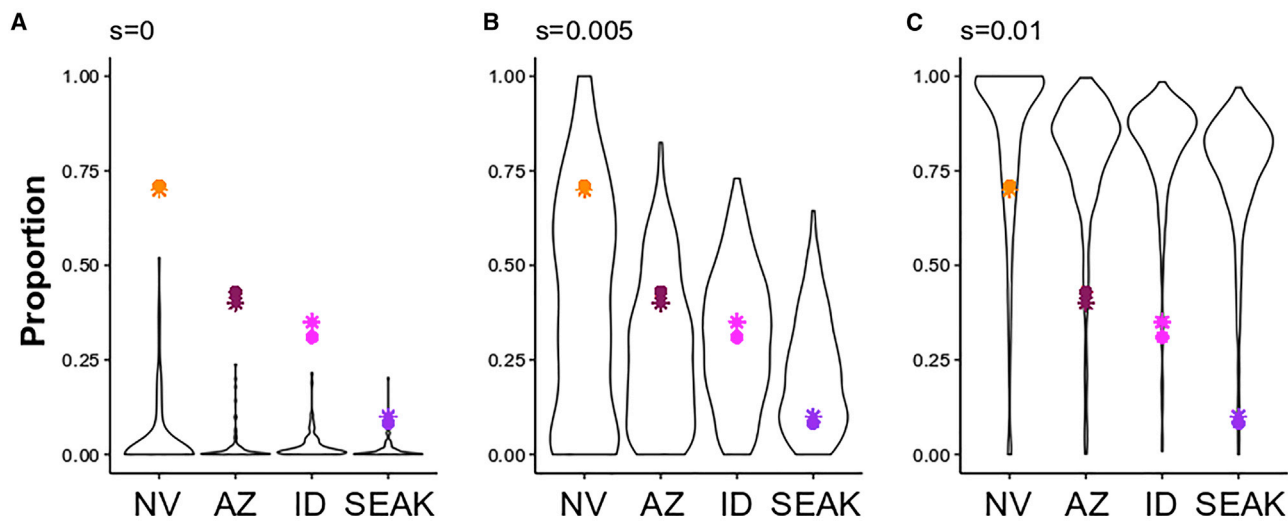


Figure 6. Simulation models of population allele frequencies under increasing selection coefficients

Simulation models for the frequency of a derived allele ($h = 0.75$) following 1,440 generations in four populations of *Ursus americanus* (NV, Nevada; AZ, Arizona; ID, Idaho; SEAK, Southeast Alaska) connected via gene flow (see Figure S6). Models varied by selection coefficients (s ; A, 0; B, 0.005; C, 0.01) and accounted for population expansion and bottlenecks. Each simulation model was run for 1,000 iterations, and panels represent runs in which the derived allele did not go extinct within a run; thus, sample size varies (A, 95; B, 394; C, 614). Colored points represent R153C genotypic frequencies (circles) estimated in this study for each respective population or phenotypic frequencies (stars) inferred from contour maps.⁵ See also Figure S6.

(WGS) of six individuals, which estimated that divergence between the western and eastern lineages began 100 kya with cessation of gene flow 22 kya (Figures 5A and 5B). Taken together with additional coalescent and range expansion analyses (Figure S3), our results suggest that R153C arose in a western lineage population of *U. americanus* and spread via gene flow across the range (Figure 5C), including contemporary eastward movement too young to be captured using these coalescent estimates.

Selection analyses

We used population genetic modeling and simulations to investigate whether clinal variation of R153C allele frequency was more likely to be explained by selection or genetic drift. We compared models with a range of dominance (h) and selection (s) coefficients. As depicted in Figure 6, the clinal pattern of allele frequencies was most consistent with weak selection ($0.005 < s < 0.01$) and was unlikely to be explained by genetic drift ($s = 0$). Despite the long haplotype carrying the derived *TYRP1*^{R153C} allele, there was no statistical evidence for a selective sweep (Figures S4 and S5), likely due to the combination of weak selection and low effective population size within the southwest population. In humans, *SLC24A5* drives the main axis of geographic color variation in Caucasians and has a large s of 0.16,²⁸ although other genes, *TYRP1* among them, have weaker coefficients of 0.01–0.05.^{28,29}

Two hypotheses about the selective forces acting upon the cinnamon morph of *U. americanus* have been proposed. First, lighter coloration aids in thermoregulation of bears in the hotter and/or drier climates of the southwest; second, the cinnamon morph is mimetic with *U. arctos* where these species are sympatric. We used BayEnv2³⁰ to test for correlation between R153C

allele frequency and climate, geography, or the presence/absence of *U. arctos* prior to anthropogenic extirpation, but we identified no notable Bayes factors (Table S4). Although this approach cannot rigorously exclude thermoregulation or mimicry as a force driving selection, it is possible that an additional, as yet untested mechanism underlies weak selection such as crypsis in open canopy environments. For example, individuals color matched within their environment has been suggested to decrease infanticide and/or predation in the Giant Panda.³¹

Implications for infraspecific taxonomy in American black bears

Historically, brown coat color has been used as a defining phenotype for delimiting 4 of the 16 *U. americanus* subspecies: *U. a. amblyceps* (southwest/southern Rocky Mountains), *U. a. cinnamomum* (northern Rocky Mountains), *U. a. luteolus* (Louisiana), and *U. a. machetes* (western Mexico).^{32–34} Further, the original description of *U. luteolus* from 1821³³ notes the cinnamon morph ranging from Virginia to Louisiana, where it is not presently found. Our results indicate that the geographic distribution of brown coats is being driven by recent and ongoing gene flow, suggesting that cinnamon morphs will increase in frequency within the eastern lineage in the future. We suggest that the young age of the causative variant and rapid spread via gene flow make this a poor character trait for infraspecific delimitation.

Conclusion

Here, we show that the cinnamon morph of the American black bear shares phenotypic similarity with brown bears in their coat coloration, and we demonstrate that eumelanin dilution causes this similarity. We identified two independently evolved and species-specific alleles within *TYRP1* that result in Arg to Cys

residue changes that disrupt protein localization to the melanosome. Our functional assay shows that the *U. arctos* R114C change has a greater effect on pigment production in melan-b cells than the *U. americanus* R153C, yet R114C has not fixed within the species (Figure S2B), suggesting it may modify color without being the initial causative locus. By contrast, the *U. americanus* R153C is responsible for most color variation within the species. Neither variant appears detrimental to fitness in bears unlike in humans with OCA3; instead, R153C appears to be under weak positive selection. Cryptic as an adaptive mechanism has generally explained why prey species and ambush predators color match within their environments; here, we suggest cryptic as a broader adaptive mechanism for large-bodied species.

STAR★METHODS

Detailed methods are provided in the online version of this paper and include the following:

- KEY RESOURCES TABLE
- RESOURCE AVAILABILITY
 - Lead contact
 - Materials availability
 - Data and code availability
- EXPERIMENTAL MODEL AND SUBJECT DETAILS
- METHOD DETAILS
 - Sample collection
 - Hair analyses
 - Whole genome sequencing and variant calling
- QUANTIFICATION AND STATISTICAL ANALYSIS
 - Chemical analysis of hairs
 - GWAS and Haplotype Characterization
 - Candidate gene analysis
 - Genotyping TYRP1^{R153C}
 - Functional Validation of TYRP1 Alleles
 - Allele age
 - Demography
 - Selection tests
 - Gene flow simulation

SUPPLEMENTAL INFORMATION

Supplemental information can be found online at <https://doi.org/10.1016/j.cub.2022.11.042>.

ACKNOWLEDGMENTS

We thank Omar Skalli for microscopy training, Jay Puckett for assistance with maps, and two anonymous reviewers for comments that improved the manuscript. E.E.P., I.S.D., and M.D.P. were supported by funds from the University of Memphis. C.B.K. and G.S.B. were supported by NIH R01 AR067925 and the HudsonAlpha Institute. M.S.M. and D.C.H. were supported by NIH R01 AR0076241. A.P. was supported by NIH R35 GM134957-01 and American Diabetes Association Pathway to Stop Diabetes grant 1-19-VSN-02. Any use of trade, firm, or product names is for descriptive purposes only and does not imply endorsement by the U.S. Government.

AUTHOR CONTRIBUTIONS

Conceptualization, E.E.P. and G.S.B. (lead) and M.S.M. and C.B.K. (supporting); data curation, E.E.P. (lead) and M.D.P. (supporting); formal analyses,

E.E.P. (lead) and M.S.M. (supporting); investigation, E.E.P. (lead) and I.S.D., D.C.H., K.W., G.B., S.I., and M.R. (supporting); methodology, E.E.P., C.B.K., and G.S.B. (equal) and K.M. and A.P. (supporting); project administration, E.E.P. and G.S.B. (equal); resources, J.L.B., D.E.B., C.C., A.P.C., M.D., C.S.D., N.F., N.L.F., D.L.G., N.G., K.G., M.H., D.K., C.L., R.L., C.L.-R., T.L., A.L., C.O., M.O., H.R., J.L.S., S.K.S., J.S., S.T., F.v.M., C.W., R.W., and F.W. (equal); supervision, G.S.B. (lead) and E.E.P. and M.S.M. (supporting); visualization, E.E.P. (lead), M.S.M. (equal), and G.S.B. (supporting); writing – original draft, E.E.P., G.S.B., and M.S.M. (equal) and G.B. (supporting); writing – review & editing, all authors.

DECLARATION OF INTERESTS

The authors declare no competing interests.

Received: September 14, 2022

Revised: November 8, 2022

Accepted: November 18, 2022

Published: December 16, 2022

REFERENCES

1. Hoekstra, H.E., Hirschmann, R.J., Bunday, R.A., Insel, P.A., and Crossland, J.P. (2006). A single amino acid mutation contributes to adaptive beach mouse color pattern. *Science* 313, 101–104. <https://doi.org/10.1126/science.1126121>.
2. Basu Mallick, C., Iliescu, F.M., Möls, M., Hill, S., Tamang, R., Chaubey, G., Goto, R., Ho, S.Y.W., Gallego Romero, I., Crivellaro, F., et al. (2013). The light skin allele of *SLC24A5* in South Asians and Europeans shares identity by descent. *PLoS Genet.* 9, e1003912. <https://doi.org/10.1371/journal.pgen.1003912>.
3. Benjamin-Fink, N., and Reilly, B.K. (2017). Conservation implications of wildlife translocations; the state's ability to act as conservation units for wildebeest populations in South Africa. *Glob. Ecol. Conserv.* 12, 46–58. <https://doi.org/10.1016/j.gecco.2017.08.008>.
4. Wikipedia (2021). The cinnamon bear. https://en.wikipedia.org/wiki/The_Cinnamon_Bear.
5. Rounds, R.C. (1987). Distribution and analysis of colourmorphs of the black bear (*Ursus americanus*). *J. Biogeogr.* 14, 521–538.
6. Pedersen, M.W., De Sanctis, B., Saremi, N.F., Sikora, M., Puckett, E.E., Gu, Z., Moon, K.L., Kapp, J.D., Vinner, L., Vardanyan, Z., et al. (2021). Environmental genomics of Late Pleistocene black bears and giant short-faced bears. *Curr. Biol.* 31, 2728–2736.e8. <https://doi.org/10.1016/j.cub.2021.04.027>.
7. Puckett, E.E., Etter, P.D., Johnson, E.A., and Eggert, L.S. (2015). Phylogeographic analyses of American black bears (*Ursus americanus*) suggest four glacial refugia and complex patterns of post-glacial admixture. *Mol. Biol. Evol.* 32, 2338–2350.
8. Ito, S., Del Bino, S., Hirobe, T., and Wakamatsu, K. (2020). Improved HPLC conditions to determine eumelanin and pheomelanin contents in biological samples using an ion pair reagent. *Int. J. Mol. Sci.* 21, 5134.
9. Ito, S., Nakanishi, Y., Valenzuela, R.K., Brilliant, M.H., Kolbe, L., and Wakamatsu, K. (2011). Usefulness of alkaline hydrogen peroxide oxidation to analyze eumelanin and pheomelanin in various tissue samples: application to chemical analysis of human hair melanins. *Pigment Cell Melanoma Res.* 24, 605–613. <https://doi.org/10.1111/j.1755-148X.2011.00864.x>.
10. Srivastava, A., Kumar Sarsani, V., Fiddes, I., Sheehan, S.M., Seger, R.L., Barter, M.E., Neptune-Bear, S., Lindqvist, C., and Korstanje, R. (2019). Genome assembly and gene expression in the American black bear provides new insights into the renal response to hibernation. *DNA Res.* 26, 37–44. <https://doi.org/10.1093/dnares/dsy036>.
11. Rubinacci, S., Ribeiro, D.M., Hofmeister, R.J., and Delaneau, O. (2021). Efficient phasing and imputation of low-coverage sequencing data using large reference panels. *Nat. Genet.* 53, 120–126. <https://doi.org/10.1038/s41588-020-00756-0>.

12. Zhou, X., and Stephens, M. (2012). Genome-wide efficient mixed-model analysis for association studies. *Nat. Genet.* **44**, 821–824. <https://doi.org/10.1038/ng.2310>.
13. Marnetto, D., and Huerta-Sánchez, E. (2017). Haplostrips: revealing population structure through haplotype visualization. *Methods Ecol. Evol.* **8**, 1389–1392. <https://doi.org/10.1111/2041-210X.12747>.
14. Barrett, J.C., Fry, B., Maller, J., and Daly, M.J. (2005). Haploview: analysis and visualization of LD and haplotype maps. *Bioinformatics* **21**, 263–265. <https://doi.org/10.1093/bioinformatics/bth457>.
15. Lai, X., Wichers, H.J., Soler-Lopez, M., and Dijkstra, B.W. (2017). Structure of human tyrosinase related protein 1 reveals a binuclear zinc active site important for melanogenesis. *Angew. Chem. Int. Ed. Engl.* **56**, 9812–9815. <https://doi.org/10.1002/anie.201704616>.
16. Manga, P., Kromberg, J.G.R., Box, N.F., Sturm, R.A., Jenkins, T., and Ramsay, M. (1997). Rufous oculocutaneous albinism in southern African blacks is caused by mutations in the TYRP1 gene. *Am. J. Hum. Genet.* **61**, 1095–1101. <https://doi.org/10.1086/301603>.
17. Lasseaux, E., Plaisant, C., Michaud, V., Pennamen, P., Trimouille, A., Gaston, L., Monfermé, S., Lacombe, D., Rooryck, C., Morice-Picard, F., and Arveiler, B. (2018). Molecular characterization of a series of 990 index patients with albinism. *Pigment Cell Melanoma Res.* **31**, 466–474. <https://doi.org/10.1111/pcmr.12688>.
18. Karczewski, K.J., Francioli, L.C., Tiao, G., Cummings, B.B., Alföldi, J., Wang, Q., Collins, R.L., Laricchia, K.M., Ganna, A., Birnbaum, D.P., et al. (2020). The mutational constraint spectrum quantified from variation in 141,456 humans. *Nature* **581**, 434–443. <https://doi.org/10.1038/s41586-020-2308-7>.
19. Landrum, M.J., Lee, J.M., Benson, M., Brown, G.R., Chao, C., Chitipiralla, S., Gu, B., Hart, J., Hoffman, D., Jang, W., et al. (2018). ClinVar: improving access to variant interpretations and supporting evidence. *Nucleic Acids Res.* **46**, D1062–D1067. <https://doi.org/10.1093/nar/gkx1153>.
20. Smith, J.R., Hayman, G.T., Wang, S.-J., Laulederkind, S.J.F., Hoffman, M.J., Kaldunski, M.L., Tutaj, M., Thota, J., Nalabolu, H.S., Ellanki, S.L.R., et al. (2020). The year of the rat: the Rat Genome Database at 20: a multi-species knowledgebase and analysis platform. *Nucleic Acids Res.* **48**, D731–D742. <https://doi.org/10.1093/nar/gkz1041>.
21. Raposo, G., Tenza, D., Murphy, D.M., Berson, J.F., and Marks, M.S. (2001). Distinct protein sorting and localization to premelanosomes, melanosomes, and lysosomes in pigmented melanocytic cells. *J. Cell Biol.* **152**, 809–824. <https://doi.org/10.1083/jcb.152.4.809>.
22. Seiji, M., Fitzpatrick, T.B., and Birbeck, M.S. (1961). The melanosome: a distinctive subcellular particle of mammalian melanocytes and the site of melanogenesis. *J. Invest. Dermatol.* **36**, 243–252.
23. Groux-Degroote, S., Van Dijk, S.M., Wolthoorn, J., Neumann, S., Theos, A.C., De Mazière, A.M., Klumperman, J., Van Meer, G., and Sprong, H. (2008). Glycolipid-dependent sorting of melanosomal from lysosomal membrane proteins by luminal determinants. *Traffic* **9**, 951–963. <https://doi.org/10.1111/j.1600-0854.2008.00740.x>.
24. Smith, K.G., and Clark, J.D. (1994). Black bears in Arkansas: characteristics of a successful translocation. *J. Mammal.* **75**, 309–320. <https://doi.org/10.2307/1382549>.
25. Puckett, E.E., Kristensen, T.V., Wilton, C.M., Lyda, S.B., Noyce, K.V., Holahan, P.M., Leslie, D.M., Beringer, J., Belant, J.L., White, D., Jr., and Eggert, L.S. (2014). Influence of drift and admixture on population structure of American black bears (*Ursus americanus*) in the Central Interior Highlands, USA, 50 years after translocation. *Mol. Ecol.* **23**, 2414–2427.
26. Platt, A., Pivrotto, A., Knoblach, J., and Hey, J. (2019). An estimator of first coalescent time reveals selection on young variants and large heterogeneity in rare allele ages among human populations. *PLoS Genet.* **15**, e1008340. <https://doi.org/10.1371/journal.pgen.1008340>.
27. Wang, K., Mathieson, I., O’Connell, J., and Schiffels, S. (2020). Tracking human population structure through time from whole genome sequences. *PLoS Genet.* **16**, e1008552. <https://doi.org/10.1371/journal.pgen.1008552>.
28. Beleza, S., Johnson, N.A., Candille, S.I., Absher, D.M., Coram, M.A., Lopes, J., Campos, J., Araújo, I.I., Anderson, T.M., Vilhjálmsson, B.J., et al. (2013). Genetic architecture of skin and eye color in an African-European admixed population. *PLoS Genet.* **9**, e1003372. <https://doi.org/10.1371/journal.pgen.1003372>.
29. Wilde, S., Timpson, A., Kirsanow, K., Kaiser, E., Kayser, M., Unterländer, M., Hoffelder, N., Potekhina, I.D., Schier, W., Thomas, M.G., and Burger, J. (2014). Direct evidence for positive selection of skin, hair, and eye pigmentation in Europeans during the last 5,000 y. *Proc. Natl. Acad. Sci. USA* **111**, 4832–4837. <https://doi.org/10.1073/pnas.1316513111>.
30. Günther, T., and Coop, G. (2013). Robust identification of local adaptation from allele frequencies. *Genetics* **195**, 205–220. <https://doi.org/10.1534/genetics.113.152462>.
31. Nokelainen, O., Scott-Samuel, N.E., Nie, Y., Wei, F., and Caro, T. (2021). The giant panda is cryptic. *Sci. Rep.* **11**, 21287. <https://doi.org/10.1038/s41598-021-00742-4>.
32. Baird, S.F. (1859). *Mammals of the boundary. Report on the United States and Mexican boundary survey: made under the Direction of the Secretary of the Interior*, pp. 1–62.
33. Griffith, E. (1821). *General and Particular Descriptions of the Vertebrated Animals: Order Carnivora* (Baldwin, Cradock, and Joy).
34. Elliot, D.G. (1903). *Descriptions of apparently new species of mammals of the genera Heteromys and Ursus from Mexico and Washington. Field Columbian Museum Publications, Zoology Series 380*, pp. 233–237.
35. Liu, S., Lorenzen, E.D., Fumagalli, M., Li, B., Harris, K., Xiong, Z., Zhou, L., Korneliusson, T.S., Somel, M., Babbitt, C., et al. (2014). Population genomics reveal recent speciation and rapid evolutionary adaptation in polar bears. *Cell* **157**, 785–794. <https://doi.org/10.1016/j.cell.2014.03.054>.
36. Benazzo, A., Trucchi, E., Cahill, J.A., Maisano Delsler, P., Mona, S., Fumagalli, M., et al. (2017). Survival and divergence in a small group: the extraordinary genomic history of the endangered Apennine brown bear stragglers. *Proc. Natl. Acad. Sci. USA* **114**, E9589–E9597. <https://doi.org/10.1073/pnas.1707279114>.
37. Cahill, J.A., Green, R.E., Fulton, T.L., Stiller, M., Jay, F., Ovsyanikov, N., Salamzade, R., St. John, J., Stirling, I., Slatkin, M., and Shapiro, B. Genomic evidence for island population conversion resolves conflicting theories of polar bear evolution. *PLoS Genet.* **2013**; **9**, e1003345. <https://doi.org/10.1371/journal.pgen.1003345>.
38. Miller, W., Schuster, S.C., Welch, A.J., Ratan, A., Bedoya-Reina, O.C., Zhao, F., et al. (2012). Polar and brown bear genomes reveal ancient admixture and demographic footprints of past climate change. *Proc. Natl. Acad. Sci. USA* **109**, E2382–E2390. <https://doi.org/10.1073/pnas.1210506109>.
39. Cahill, J.A., Stirling, I., Kistler, L., Salamzade, R., Ersmark, E., Fulton, T.L., et al. (2015). Genomic evidence of geographically widespread effect of gene flow from polar bears into brown bears. *Mol. Ecol.* **24**, 1205–1217. <https://doi.org/10.1111/mec.13038>.
40. Endo, Y., Osada, N., Mano, T., and Masuda, R. (2021). Demographic history of the brown bear (*Ursus arctos*) on Hokkaido Island, Japan, based on whole-genomic sequence analysis. *Genome Biol. Evol.* **13**, evab195. <https://doi.org/10.1093/gbe/evab195>.
41. Browning, S.R., and Browning, B.L. (2007). Rapid and accurate haplotype phasing and missing-data inference for whole-genome association studies by use of localized haplotype clustering. *Am. J. Hum. Genet.* **81**, 1084–1097. <https://doi.org/10.1086/521987>.
42. Gabriel, S.B., Schaffner, S.F., Nguyen, H., Moore, J.M., Roy, J., Blumenstiel, B., Higgins, J., DeFelice, M., Lochner, A., Faggart, M., et al. (2002). The structure of haplotype blocks in the human genome. *Science* **296**, 2225–2229. <https://doi.org/10.1126/science.1069424>.
43. Taylor, G.A., Kirk, H., Coombe, L., Jackman, S.D., Chu, J., Tse, K., Cheng, D., Chuah, E., Pandoh, P., Carlsen, R., et al. (2018). *The genome of the North American brown bear or grizzly: Ursus arctos ssp. horribilis*. *Genes* **9**, 598.
44. Altschul, S.F., Gish, W., Miller, W., Myers, E.W., and Lipman, D.J. (1990). Basic local alignment search tool. *J. Mol. Biol.* **215**, 403–410. [https://doi.org/10.1016/S0022-2836\(05\)80360-2](https://doi.org/10.1016/S0022-2836(05)80360-2).

45. Zhang, Z., Schwartz, S., Wagner, L., and Miller, W. (2000). A greedy algorithm for aligning DNA sequences. *J. Comput. Biol.* **7**, 203–214. <https://doi.org/10.1089/10665270050081478>.
46. Li, H., Handsaker, B., Wysoker, A., Fennell, T., Ruan, J., Homer, N., Marth, G., Abecasis, G., and Durbin, R.; 1000 Genome Project Data Processing Subgroup (2009). The Sequence Alignment/Map format and SAMtools. *Bioinformatics* **25**, 2078–2079. <https://doi.org/10.1093/bioinformatics/btp352>.
47. Ng, P.C., and Henikoff, S. (2003). SIFT: predicting amino acid changes that affect protein function. *Nucleic Acids Res.* **31**, 3812–3814. <https://doi.org/10.1093/nar/gkg509>.
48. Choi, Y., Sims, G.E., Murphy, S., Miller, J.R., and Chan, A.P. (2012). Predicting the functional effect of amino acid substitutions and indels. *PLoS One* **7**, e46688. <https://doi.org/10.1371/journal.pone.0046688>.
49. Adzhubei, I.A., Schmidt, S., Peshkin, L., Ramensky, V.E., Gerasimova, A., Bork, P., Kondrashov, A.S., and Sunyaev, S.R. (2010). A method and server for predicting damaging missense mutations. *Nat. Methods* **7**, 248–249. <https://doi.org/10.1038/nmeth0410-248>.
50. Geneious Prime (2019). Geneious Prime. <https://www.geneious.com/download/previous-versions/>.
51. R Core Team (2020). R: a language and environment for statistical computing (R Foundation for Statistical Computing).
52. Setty, S.R.G., Tenza, D., Truschel, S.T., Chou, E., Sviderskaya, E.V., Theos, A.C., Lamoreux, M.L., Di Pietro, S.M.D., Starcevic, M., Bennett, D.C., et al. (2007). BLOC-1 is required for cargo-specific sorting from vacuolar early endosomes toward lysosome-related organelles. *Mol. Biol. Cell* **18**, 768–780. <https://doi.org/10.1091/mbc.e06-12-1066>.
53. Bennett, D.C., Cooper, P.J., Dexter, T.J., Devlin, L.M., Heasman, J., and Nester, B. (1989). Cloned mouse melanocyte lines carrying the germline mutations albino and brown: complementation in culture. *Development* **105**, 379–385.
54. Bennett, D.C., Huszar, D., Laipis, P.J., Jaenisch, R., and Jackson, I.J. (1990). Phenotypic rescue of mutant brown melanocytes by a retrovirus carrying a wild-type tyrosinase-related protein gene. *Development* **110**, 471–475.
55. Morita, S., Kojima, T., and Kitamura, T. (2000). Plat-E: an efficient and stable system for transient packaging of retroviruses. *Gene Ther.* **7**, 1063–1066.
56. Dennis, M.K., Delevoe, C., Acosta-Ruiz, A., Hurbain, I., Romao, M., Hesketh, G.G., Goff, P.S., Sviderskaya, E.V., Bennett, D.C., Luzio, J.P., et al. (2016). BLOC-1 and BLOC-3 regulate VAMP7 cycling to and from melanosomes via distinct tubular transport carriers. *J. Cell Biol.* **214**, 293–308. <https://doi.org/10.1083/jcb.201605090>.
57. Meng, R., Wang, Y., Yao, Y., Zhang, Z., Harper, D.C., Heijnen, H.F.G., Sitaram, A., Li, W., Raposo, G., Weiss, M.J., et al. (2012). SLC35D3 delivery from megakaryocyte early endosomes is required for platelet dense granule biogenesis and is differentially defective in Hermansky-Pudlak syndrome models. *Blood* **120**, 404–414.
58. Bowman, S.L., Le, L., Zhu, Y., Harper, D.C., Sitaram, A., Theos, A.C., Sviderskaya, E.V., Bennett, D.C., Raposo-Benedetti, G., Owen, D.J., et al. (2021). A BLOC-1-AP-3 super-complex sorts a cis-SNARE complex into endosome-derived tubular transport carriers. *J. Cell Biol.* **220**, e202005173. <https://doi.org/10.1083/jcb.202005173>.
59. Delevoe, C., Hurbain, I., Tenza, D., Sibarita, J.-B., Uzan-Gafsou, S., Ohno, H., Geerts, W.J.C., Verkleij, A.J., Salamero, J., Marks, M.S., and Raposo, G. (2009). AP-1 and KIF13A coordinate endosomal sorting and positioning during melanosome biogenesis. *J. Cell Biol.* **187**, 247–264. <https://doi.org/10.1083/jcb.200907122>.
60. Catchen, J., Hohenlohe, P.A., Bassham, S., Amores, A., and Cresko, W.A. (2013). STACKS: an analysis tool set for population genomics. *Mol. Ecol.* **22**, 3124–3140. <https://doi.org/10.1111/mec.12354>.
61. Chang, C.C., Chow, C.C., Tellier, L.C.A.M., Vattikuti, S., Purcell, S.M., and Lee, J.J. (2015). Second-generation PLINK: rising to the challenge of larger and richer datasets. *GigaScience* **4**, 7. <https://doi.org/10.1186/s13742-015-0047-8>.
62. Purcell, S., Neale, B., Todd-Brown, K., Thomas, L., Ferreira, M.A.R., Bender, D., Maller, J., Sklar, P., de Bakker, P.I.W., Daly, M.J., and Sham, P.C. (2007). PLINK: a tool set for whole-genome association and population-based linkage analyses. *Am. J. Hum. Genet.* **81**, 559–575. <https://doi.org/10.1086/519795>.
63. Puckett, E.E. (2015). Phylogeography and population genomics of the American black bear (*Ursus americanus*) (University of Missouri).
64. Schneider, C.A., Rasband, W.S., and Eliceiri, K.W. (2012). NIH Image to ImageJ: 25 years of image analysis. *Nat. Methods* **9**, 671–675. <https://doi.org/10.1038/nmeth.2089>.
65. Li, H., and Durbin, R. (2010). Fast and accurate long-read alignment with Burrows-Wheeler transform. *Bioinformatics* **26**, 589–595. <https://doi.org/10.1093/bioinformatics/btp698>.
66. McKenna, A., Hanna, M., Banks, E., Sivachenko, A., Cibulskis, K., Kernysky, A., Garimella, K., Altshuler, D., Gabriel, S., Daly, M., and DePristo, M.A. (2010). The Genome Analysis Toolkit: a MapReduce framework for analyzing next-generation DNA sequencing data. *Genome Res.* **20**, 1297–1303. <https://doi.org/10.1101/gr.107524.110>.
67. Li, H. (2011). A statistical framework for SNP calling, mutation discovery, association mapping and population genetical parameter estimation from sequencing data. *Bioinformatics* **27**, 2987–2993. <https://doi.org/10.1093/bioinformatics/btr509>.
68. Browning, B.L., Zhou, Y., and Browning, S.R. (2018). A one-penny imputed genome from next-generation reference panels. *Am. J. Hum. Genet.* **103**, 338–348. <https://doi.org/10.1016/j.ajhg.2018.07.015>.
69. Schiffels, S., and Durbin, R. (2014). Inferring human population size and separation history from multiple genome sequences. *Nat. Genet.* **46**, 919–925. <https://doi.org/10.1038/ng.3015>.
70. Li, H. (2009). SNPable Regions. <https://lh3h3.users.sourceforge.net/snpable.shtml>.
71. Kumar, S., and Subramanian, S. (2002). Mutation rates in mammalian genomes. *Proc. Natl. Acad. Sci. USA* **99**, 803–808. <https://doi.org/10.1073/pnas.022629899>.
72. Onorato, D.P., Hellgren, E.C., Van Den Bussche, R.A., and Doan-Crider, D.L. (2004). Phylogeographic patterns within a metapopulation of black bears (*Ursus americanus*) in the American Southwest. *J. Mammal.* **85**, 140–147.
73. Peter, B.M., and Slatkin, M. (2013). Detecting range expansions from genetic data. *Evolution* **67**, 3274–3289. <https://doi.org/10.1111/evo.12202>.
74. Danecek, P., Auton, A., Abecasis, G., Albers, C.A., Banks, E., DePristo, M.A., Handsaker, R.E., Lunter, G., Marth, G.T., Sherry, S.T., et al. (2011). The variant call format and VCFtools. *Bioinformatics* **27**, 2156–2158. <https://doi.org/10.1093/bioinformatics/btr330>.
75. Voight, B.F., Kudravalli, S., Wen, X., and Pritchard, J.K. (2006). A map of recent positive selection in the human genome. *PLOS Biol.* **4**, e72. <https://doi.org/10.1371/journal.pbio.0040072>.
76. Szpiech, Z.A. (2022). selscan 2.0: scanning for sweeps in unphased data. Preprint at bioRxiv. <https://doi.org/10.1101/2021.10.22.465497>.
77. Szpiech, Z.A., and Hernandez, R.D. (2014). selscan: an efficient threaded program to perform EHH-based scans for positive selection. *Mol. Biol. Evol.* **31**, 2824–2827. <https://doi.org/10.1093/molbev/msu211>.
78. Vatsiou, A.I., Bazin, E., and Gaggiotti, O.E. (2016). Detection of selective sweeps in structured populations: a comparison of recent methods. *Mol. Ecol.* **25**, 89–103. <https://doi.org/10.1111/mec.13360>.
79. Coop, G., Witonsky, D., Di Rienzo, A., and Pritchard, J.K. (2010). Using environmental correlations to identify loci underlying local adaptation. *Genetics* **185**, 1411–1423. <https://doi.org/10.1534/genetics.110.114819>.
80. Kriticos, D.J., Jarošik, V., and Ota, N. (2014). Extending the suite of bioclim variables: a proposed registry system and case study using principal components analysis. *Methods Ecol. Evol.* **5**, 956–960. <https://doi.org/10.1111/2041-210X.12244>.

81. Hutchinson, M., Xu, T., Houlder, D., Nix, H., and McMahon, J. (2009). ANUCLIM 6.0 User's Guide (Australian National University, Fenner School of Environment and Society).
82. Haroldson, M.A., Clapham, M., Costello, C.M., Gunther, K.A., Kendall, K.C., Miller, S.D., Pigeon, K.E., Proctor, M.F., Rode, K.D., Servheen, C., et al. (2021). Brown bear (*Ursus arctos*; North America). In *Bears of the World*, V.P.a.M. Melletti, ed. (Cambridge University Press).
83. Lischer, H.E.L., and Excoffier, L. (2012). PGDSpider: an automated data conversion tool for connecting population genetics and genomics programs. *Bioinformatics* 28, 298–299. <https://doi.org/10.1093/bioinformatics/btr642>.
84. Haller, B.C., and Messer, P.W. (2019). SLiM 3: forward genetic simulations beyond the Wright–Fisher model. *Mol. Biol. Evol.* 36, 632–637. <https://doi.org/10.1093/molbev/msy228>.
85. Malaney, J.L., Lackey, C.W., Beckmann, J.P., and Matocq, M.D. (2018). Natural rewilding of the Great Basin: genetic consequences of recolonization by black bears (*Ursus americanus*). *Divers. Distrib.* 24, 168–178. <https://doi.org/10.1111/ddi.12666>.

STAR★METHODS

KEY RESOURCES TABLE

REAGENT or RESOURCE	SOURCE	IDENTIFIER
Antibodies		
TA99/Mel-5	American Type Culture Collection	HB-8704
Alexafluor 488-labeled donkey anti-mouse IgG	Jackson Immunoresearch	715-545-151
Bacterial and virus strains		
E.coli-Top10	Invitrogen	C66411
Biological samples		
U. arctos- DNA sample	This study	GYE906
U. arctos- DNA sample	This study	GYE922
U. arctos- DNA sample	This study	GYE953
U. arctos- DNA sample	This study	AK17500
U. arctos- DNA sample	This study	AK17512
U. arctos- DNA sample	This study	AK17578
U. arctos- DNA sample	Liu et al. ³⁵	RF01
U. arctos- DNA sample	Liu et al. ³⁵	SJS01
U. arctos- DNA sample	Liu et al. ³⁵	OFS01
U. arctos- DNA sample	Benazzo et al. ³⁶	ALP1
U. arctos- DNA sample	Cahill et al. ³⁷	AKAdmiralty1
U. arctos- DNA sample	Miller et al. ³⁸	AKAdmiralty2
U. arctos- DNA sample	Cahill et al. ³⁷	AKAdmiralty3
U. arctos- DNA sample	Miller et al. ³⁸	AKBaranof1
U. arctos- DNA sample	Liu et al. ³⁵	AKBaranof2
U. arctos- DNA sample	Liu et al. ³⁵	AKChichagof1
U. arctos- DNA sample	Liu et al. ³⁵	AKChichagof2
U. arctos- DNA sample	Liu et al. ³⁵	AKChichagof3
U. arctos- DNA sample	Liu et al. ³⁵	AKChichagof4
U. arctos- DNA sample	Cahill et al. ³⁹	AKChichagof5
U. arctos- DNA sample	Cahill et al. ³⁷	AKDenali1
U. arctos- DNA sample	Miller et al. ³⁸	AKKenai
U. arctos- DNA sample	Benazzo et al. ³⁶	APN2
U. arctos- DNA sample	Benazzo et al. ³⁶	GRE2
U. arctos- DNA sample	Endo et al. ⁴⁰	JPHc1
U. arctos- DNA sample	Endo et al. ⁴⁰	JPHc2
U. arctos- DNA sample	Endo et al. ⁴⁰	JPHe1
U. arctos- DNA sample	Endo et al. ⁴⁰	JPHe2
U. arctos- DNA sample	Endo et al. ⁴⁰	JPHs1
U. arctos- DNA sample	Endo et al. ⁴⁰	JPHs2
U. arctos- DNA sample	Liu et al. ³⁵	MTgnp
U. arctos- DNA sample	Cahill et al. ³⁹	Dalarna, SWE
U. maritimus- DNA sample	Miller et al. ³⁸	PB1
U. maritimus- DNA sample	Miller et al. ³⁸	PB2
U. americanus- DNA sample	This study	AK17023
U. americanus- DNA sample	This study	AK17047
U. americanus- DNA sample	This study	AK17117

(Continued on next page)

Continued

REAGENT or RESOURCE	SOURCE	IDENTIFIER
U. americanus- DNA sample	This study	AZ12
U. americanus- DNA sample	This study	ID10
U. americanus- DNA sample	This study	MI334
U. americanus- DNA sample	This study	MI335
U. americanus- DNA sample	This study	MN_6083
U. americanus- DNA sample	This study	MS3783
U. americanus- DNA sample	This study	NC00417
U. americanus- DNA sample	This study	NC056
U. americanus- DNA sample	This study	NVb83
U. americanus- DNA sample	This study	NVb99
U. americanus- DNA sample	This study	NVg5
U. americanus- DNA sample	This study	WV17_01
U. americanus- DNA sample	This study	HA1
U. americanus- DNA sample	This study	HA2
U. americanus- DNA sample	This study	HA3
U. americanus- DNA sample	This study	HA4
U. americanus- DNA sample	This study	HA5
U. americanus- DNA sample	This study	HA6
U. americanus- DNA sample	This study	HA7
U. americanus- DNA sample	This study	HA8
U. americanus- DNA sample	This study	HA9

Chemicals, peptides, and recombinant proteins

BamHI	NEB	R0136L
HindIII	NEB	R0104L
XhoI	NEB	R0146L
SnaBI	NEB	R0130S
Lipofectamine 2000	Invitrogen	11668-019
Hygromycin B	Research Products International	H75020-1.0
RPMI 1640 medium	Gibco	11875-085
FBS	R&D Systems	S1150
PBS	Corning	21-031-CM
Tris-HCl	Fisher	BP153-1
EDTA	Sigma	E5134-50G
dithiothreitol	Sigma	3483-12-3
DMSO	Sigma	D2660
LB Broth	Fisher	BP1426-2
Ampicillin	Fisher	BP1760-25
Agar	Fisher	BP1423-2
Agarose	GibcoBRL	15510-027
2-log DNA Ladder	NEB	N3200L
GelGreen Nucleic Acid Stain	Biotium	41005
Tris-EDTA pH 8.0	Ambion	AM9858
Terrific Broth	Amresco	J869-5KG
Glucose	Sigma	G7528-250G
Sodium Hydroxide	Sigma	S8045
SDS	Invitrogen	15525-017
Potassium Acetate	Sigma	P1190-100G
Glacial Acetic Acid	Fisher	BP1185-500

(Continued on next page)

Continued

REAGENT or RESOURCE	SOURCE	IDENTIFIER
Critical commercial assays		
Prime Time Gene Expression (for qPCR)	Integrated DNA Technologies (IDT)	10007065
cOmplete Protease Inhibitor Cocktail Tablets	Roche	P8849
Prolong Gold Antifade Mountant	InVitrogen	P36931
Q5 High-Fidelity DNA Polymerase	NEB	M0491L
QIAquick Gel Extraction Kit	Qiagen	28704
BCA Protein Assay Kit	Pierce	23225
Deposited data		
DNA Sequencing	This study	SRA: PRJNA867575
TYRP1 mouse WT sequence	Browning and Browning ⁴¹	NM_031202.3
Crystal structure of the human TYRP1 luminal domain	NCBI Protein Data Base	PDB: 5M8L
Experimental models: Cell lines		
melan-b	Dorothy Bennett's laboratory	Gabriel et al. ⁴²
Oligonucleotides		
pBMN vector R153C primer; forward: GGGCCCTGGATA TGGCAAAGTGCACT CACCTTTATTTGT	IDT	custom oligo synthesis
pBMN vector R153C primer; reverse: ACAAATAAAGGG TGAGTTGTGCACTTTGCC ATATCCAGGGCCC	IDT	custom oligo synthesis
pBMN vector R114C primer; forward: GACACAAGTGTG GGACGTGCTGCCTGGC TGGAGAGGAGCTGC	IDT	custom oligo synthesis
pBMN vector R114C primer; reverse: GCAGCTCCTCTC CAGCCAGGACAGCACGT CCCACAGTTGTGTC	IDT	custom oligo synthesis
pBMN flanking primer; forward: CCTCTAGACTGC CGGATCCATTTAAATTCG AATTCCTGCAGG	IDT	custom oligo synthesis
pBMN flanking primer; reverse: GGAATCAAAGTTG CTTCTGGATCCCATCAAGT CATCCGTGCAG	IDT	custom oligo synthesis
qPCR TYRP1 primer; forward: CCTGAAGTCAGG AGAAACC	This paper	N/A
qPCR TYRP1 primer; reverse: CTGGTCGCAATG ACAAAC	This paper	N/A
pPCR TYRP1 reference allele probe: FAM-ATGG CGAAGCGCACAAATC-BGQ1	This paper	N/A
pPCR TYRP1 alternative allele probe: TET-ATGGCGAA GTGCACAAT-BHQ1	This paper	N/A

(Continued on next page)

Continued

REAGENT or RESOURCE	SOURCE	IDENTIFIER
Recombinant DNA		
pCDNA3-TRP1	Gift from Walter Storkus, Univ. of Pittsburgh	N/A
pBMN-I-hygro-mCherry-hSTX13	Marks laboratory	Taylor et al. ⁴³
pBMN-I-hygro	Gift from Andrew Peden, Univ. of Scheffield	Liu et al. ³⁵
Software and algorithms		
BWA v0.7.17	Altschul et al. ⁴⁴	https://github.com/lh3/bwa
GATK v4.1.8.0	Zhang et al. ⁴⁵	https://gatk.broadinstitute.org/hc/en-us
SAMTOOLS v1.9	Li et al. ⁴⁶	https://sourceforge.net/projects/samtools/files/samtools/1.9/
BCFTOOLS v1.9	Ng and Henikoff ⁴⁷	https://sourceforge.net/projects/samtools/files/samtools/1.9/
BEAGLE v5.1	Choi et al. ⁴⁸	https://faculty.washington.edu/browning/beagle/b5_1.html
GLIMPSE 1.0.0	Rubinacci et al. ¹¹	https://github.com/odelaneau/GLIMPSE/pkgs/container/GLIMPSE%2Fglimpse
GEMMA v0.98.1	Zhou and Stephens ¹²	https://github.com/genetics-statistics/GEMMA
HAPLOVIEW 4.2	Barrett et al. ¹⁴	https://www.broadinstitute.org/haploview/downloads
Haplostrips	Marnetto and Huerta-Sánchez ¹³	https://bitbucket.org/dmarnetto/haplostrips/src/master/
PROVEAN	Adzhubei et al. ⁴⁹	https://www.jcvi.org/research/provean#downloads
PolyPhen2	Geneious Prime ⁵⁰	http://genetics.bwh.harvard.edu/pph2/
SIFT	R Core Team ⁵¹	https://sift.bii.a-star.edu.sg/index.html
GENEIOUSPRIME	Setty et al. ⁵²	https://www.geneious.com/prime/
Leica LAS-X	Leica Microsystems	https://www.leica-microsystems.com/products/microscope-software/p/leica-las-x-ls/
Microvolution	Bio-Vision Technologies	N/A
FIJI – ImageJ	Bennett et al. ⁵³	https://imagej.net/software/fiji/
Adobe Photoshop v. 24.0.0	Adobe.com	https://www.adobe.com/products/photoshop/
Graphpad Prism v. 9.4.1	GraphPad.com	https://www.graphpad.com/updates/prism-900-release-notes
Pymol	Schrödinger LLC	https://pymol.org
program R v4.0.3	Bennett et al. ⁵⁴	https://www.r-project.org/
Runtc	Platt et al. ²⁶	https://github.com/jaredgk/runtc
STACKS v2.53	Morita et al. ⁵⁵	https://catchenlab.life.illinois.edu/stacks/
PLINK v1.9	Dennis et al. ⁵⁶	https://www.cog-genomics.org/plink/
MSMC2	Meng et al. ⁵⁷	https://github.com/stschiff/msmc2
SNPable	Bowman et al. ⁵⁸	https://lh3lh3.users.sourceforge.net/snpable.shtml
Rangeexpansion	Delevoe et al. ⁵⁹	https://github.com/BenjaminPeter/rangeexpansion

(Continued on next page)

Continued

REAGENT or RESOURCE	SOURCE	IDENTIFIER
selscan v2	Dennis et al. ⁵⁶	https://github.com/szpiech/selscan
BayEnv2	Günther and Coop ³⁰	https://bitbucket.org/tguenther/bayenv2_public/src/master/
PGDSpider	Catchen et al. ⁶⁰	http://www.cmpg.unibe.ch/software/PGDSpider/
SLiM v3	Chang et al. ⁶¹	https://messerlab.org/slim/
MSMC-IM	Wang et al. ²⁷	https://github.com/wangke16/MSMC-IM
Unipro UGENE v39.0	Purcell et al. ⁶²	http://ugene.net/
Other		
Matrigel	Corning	354248
Electroporator	Bio-Rad	MicroPulser
PCR	Bio-Rad Thermal Cycler	T100
Petri Dish	VWR	25384-088
Sanger Sequencing	Molecular Cloning Laboratories (MCLAB)	service
Mouse Tyrp1 WT,R114C and R153C synthesis and cloning	Synbio Technologies	custom gene synthesis
Transilluminator	Clare Chemical Research	Dark Reader

RESOURCE AVAILABILITY**Lead contact**

Further information and requests of resources should be directed to the corresponding author Emily E. Puckett (emily.puckett@memphis.edu).

Materials availability

Plasmids and cell lines are available upon request to author MSM.

Data and code availability

Sequence data has been deposited onto the NCBI SRA: PRJNA867575. This paper does not report original code.

EXPERIMENTAL MODEL AND SUBJECT DETAILS

We extracted DNA from blood or tissue from 906 *U. americanus* individuals for whole genome sequencing (WGS) or qPCR genotyping of *TYRP1*^{R153C}. DNA was extracted from an additional six *U. arctos* individuals (muscle samples) for WGS. Hair color was measured from 391 *U. americanus* and 33 *U. arctos* individuals. Animals were not maintained in the lab, see below for details.

METHOD DETAILS**Sample collection**

We partnered with state, provincial, and federal wildlife agencies, and university partners in North America which collected hair, tissue (i.e., muscle or blood), and photographs from bears that were hunter harvested, vehicle killed, or live animals captured for other research studies or management purposes. Not all samples contained all three sampling elements (hair, tissue, and photographs). Photographs of bears confirmed all samples were adults; cubs may turn from brown to black following a molt, although black to brown transitions have not been observed (personal observation DL Garshelis). Samples were collected from 2015–2020 and georeferenced. The qPCR analysis (see below) incorporated previously collected bear samples⁶³ that were also georeferenced but without phenotypic data.

Hair analyses

We mounted one awn hair from 391 individuals onto slides, then captured an image from the middle of the sample under 20x magnification using an Olympus BX63 microscope at the Integrated Microscopy Center at the University of Memphis. We viewed all

samples with transmitted light brightfield illumination, 488.3 μ s exposure time, and 185 LED brightness. We analyzed images in ImageJ⁶⁴ using the RGBMeasure function on a 46 x 46 pixel section of the hair cortex, and recorded the mean for the red, green, and blue color channels.

Whole genome sequencing and variant calling

High coverage

We sequenced 15 *U. americanus* and six *U. arctos* individuals to \sim 30x depth (key resources table). Specifically, 350bp insert libraries were prepared using the NEB Next Ultra II DNA kit, then sequenced (150bp paired-end) on an Illumina NextGen by Novogene (Chula Vista, CA). We sequenced nine additional *U. americanus* individuals to 50x depth using Illumina HiSeqX at HudsonAlpha (Huntsville, AL). We also downloaded 26 *U. arctos* and two *U. maritimus* WGS from the NCBI SRA to use in downstream analyses (key resources table). For all species, we mapped reads to the *U. americanus* reference genome¹⁰ using BWA-MEM v0.7.17⁶⁵ with default parameters. We marked duplicates, then called variants for each sample using the GenotypeGVCFs function in GATK v4.1.8.0⁶⁶ where we set the heterozygosity parameter to 5.0×10^{-4} . For each species, we combined the samples using CombineGVCFs before joint genotyping using GenotypeGVCFs in GATK. We filtered the dataset using BCFTOOLS v1.9⁶⁷ by requiring minimum and maximum depth (-i 'MIN (FMT/DP) > 4 & MAX (FMT/DP) < 300'), minimum quality score (-i FMT/GQ >= 30), and biallelic SNPs (-m 2 -M 2 -v snps). The total number of SNPs for *U. americanus* was 8,885,511. We phased the data from each species separately using BEAGLE v5.1.^{68,41}

Low coverage

We sequenced 166 *U. americanus* animals to an average of 1.3x depth. Specifically, we followed the manufacturer's instructions for the Illumina DNA Prep Kit except that we diluted the reactions to 20% volume and started with 20 ng of genomic DNA. Two pooled libraries were constructed and each was sequenced on one lane of an Illumina 4000 at Novogene (Davis, CA). We mapped reads to the *U. americanus* reference and called variants as described above. The draft *U. americanus* (2n = 74) genome was assembled into 94,016 scaffolds; we analyzed the longest 36 scaffolds (and removed the X chromosome, HiC_scaffold_1). We used our high coverage WGS samples as a reference panel for joint imputation and phasing of the low coverage data using GLIMPSE.¹¹

QUANTIFICATION AND STATISTICAL ANALYSIS

Chemical analysis of hairs

We quantified the amount of eumelanin and pheomelanin in 13 *U. americanus* and three *U. arctos* individuals. Samples were selected based on both geographic location and visual inspection of hair color under a compound microscope to select for observed variation (*U. americanus*: black = 9; brown = 4; *U. arctos*: dark brown = 2, brown = 1). We followed the melanin determination protocols.^{8,9} Eumelanin and pheomelanin concentrations are reported as the concentrations of PTCA (pyrrole-2,3,5-tricarboxylic acid) and TTCA (thiazole-2,4,5-tricarboxylic acid) which are, respectively, the specific degradation products for each melanin. We plotted the figure in Figures 1B and 1C and report ANOVA results in the figure legend.

GWAS and Haplotype Characterization

To identify loci associated with the brown phenotype, we ran GEMMA v0.98.1.¹² Specifically, we combined our high and imputed low coverage datasets, then used the quantitative hair reflectance values (green channel of RGB measurement) as the phenotype (n = 151). We ran a principal components analysis (PCA) on the relatedness matrix created within GEMMA, and used the first two PC axes as covariates to account for population structure in the analysis. Our GWAS resulted in 23 genomic regions with *P*-values lower than 10^{-8} , although a single peak stood out and contained a known pigmentation gene, *TYRP1* (Table S2). To test if additional loci beyond *TYRP1* influenced quantitative color phenotypes in black bears, we reran the analysis using the R153C genotype from the qPCR (see below) as a third covariate. This analysis did not reveal additional loci that contributed to the coloration phenotype.

We estimated the length of the haplotype containing the derived allele within the Nevada population using HAPLOVIEW¹⁴ using the default algorithm for estimating linkage disequilibrium (LD).⁴² We then viewed this region of the genome for all samples using HAPLOSTRIPS¹³ (Figure S1). The Nevada population was selected based on the *runtc* (see below and Figure S3A) analyses which indicated it was geographically near the source population for the R153C *TYRP1* population.

Candidate gene analysis

To evaluate deleterious protein coding variation in bears, we downloaded coding sequences (CDS) for 13 candidate coat color genes (*ASIP*, *CBD103*, *EDNRB*, *KIT*, *KITLG*, *MC1R*, *MLPH*, *OCA2*, *PMEL*, *SLC24A5*, *SLC45A2*, *TYR*, *TYRP1*, and *TYRP2*) from the dog genome (*Canis familiaris*; CanFam3.1). Exons were queried against genome assemblies of *U. americanus*, *U. arctos*, and *U. maritimus*^{10,43,35} using the blastn and dc-megablast versions of NCBI BLAST+.^{44,45} We extracted the resulting sequences from the phased genome assemblies using SAMTOOLS v1.9⁴⁶ and BCFTOOLS and concatenated exons to form haplotypes. We translated each haplotype and identified missense and nonsense polymorphisms within *U. americanus*, between *U. americanus* and four *U. arctos* samples, and between *U. arctos* and *U. maritimus*. We tested each variant for deleterious effects using PROVEAN, PolyPhen2, and SIFT⁴⁷⁻⁴⁹ (Table S3). For any variant where two of the programs predicted a deleterious variant, we identified the individuals and coat color phenotypes of those animals to assess if there was concordance between *U. americanus* animals with

brown coats and the alternate allele. Only the previously identified *TYRP1*^{R153C} showed such a concordance. We constructed a neighbor joining tree from the haplotypes (with introns) using GENEIOUSPRIME⁵⁰ to visualize the gene tree.

To understand the location of the arginine to cysteine amino acid changes within the native TYRP1 protein, we input the X-ray crystal structure of the human TYRP1 luminal domain (PDB ID: 5M8L, ref Lai et al.¹⁵) into PyMol v2.5, displayed it as a ribbon diagram to emphasize alpha helices, beta sheets, and loops, and then highlighted the following features: the location of R114 and R153 amino acids (expressed in atom format), cysteines and corresponding disulfide bonds throughout the protein, and the zinc cofactors.

Genotyping *TYRP1*^{R153C}

We genotyped 906 *U. americanus* samples for the *TYRP1*^{R153C} variant using a qPCR assay.

The primers included (5' to 3'):

F: CCTTGAAGTCAGGAGAAACC

R: CTGGTCGCAATGACAAAC

The probes included (5' to 3'):

reference allele probe: FAM-ATGGCGAAGCGCACAAATTC-BGQ1

alternate allele probe: TET-ATGGCGAAGTGCACAAT-BHQ1

Primers and probes were ordered from IDT (Coralville, IA). Reaction conditions had final primer and probe concentrations of 1 μM and 0.2 μM, respectively. The thermocycler conditions in a BioRAD CFX96 included: 95°C for 3min, and 40 cycles of 95°C for 15sec then 57.9°C for 30sec. For samples where both hair color phenotypes and R153C genotypes were available (n = 317), we tested if reflectance was significantly different between genotypes using two-sided t-tests in R v3.6.0⁵¹ and report results in the legend of Figure 4.

Functional Validation of *TYRP1* Alleles

To test if the *TYRP1* variants we identified in American black (R153C) and brown (R114C) bears caused a change in pigmentation phenotype, we first used site-specific mutagenesis to generate recombinant retroviruses to co-express wildtype (WT) or variant versions of human and mouse TYRP1 with a drug resistance marker for stable cell line selection. Specifically, we first subcloned a WT *TYRP1* cDNA based on the human sequence (pCDNA3-TRP1, a gift to MS Marks from W Storkus, University of Pittsburgh, Pittsburgh, PA, USA) into the pBMN-I-Hygro retroviral vector.⁵² The R153C and R114C variants were generated individually by overlapping PCR using synthetic oligonucleotides bearing the desired mutations (denoted by asterisks [*] in the sequences below).

The oligos for R153C were (5' to 3'):

F: GGGCCCTGGATATGGCAAAGT*GCACAACTCACCCCTTTATTTGT

R: ACAATAAAGGGTGAGTTGTGCA*CTTTGCCATATCCAGGGCCC

The oligos for R114C were (5' to 3'):

F: GACACAACTGTGGGACGTGCT*GTCCTGGCTGGAGAGGAGCTGC

R: GCAGCTCCTCTCCAGCCAGGACA*GCACGTCCCACAGTTGTGTC

The flanking oligos for both products were (5' to 3'):

F: CCTCTAGACTGCCGGATCCATTTAAATTCTGAATTCCTGCAGG

R: GGAATCAAAGTTGCTTCTGGATCCCATCAAGTCATCCGTGCAG

The R153C mutation was generated by combining a 707bp and a 386bp product to obtain a 1,050bp product. The R114C mutation was generated by combining a 590bp and a 503bp product to obtain a 1,050bp product. The PCR products bearing the mutations were cloned individually as 1,013bp BamHI fragments into the BamHI site in the pBMN-I-Hygro-hTYRP1 construct after excising the WT BamHI fragment. The clones bearing the correctly oriented fragments were selected by HindIII restriction and confirmed by Sanger sequencing the BamHI junctions. The generated mutations were confirmed by Sanger sequencing.

The WT mouse *TYRP1* cDNA sequence (NCBI accession NM_031202.3) was also used to generate the mutant forms. The three versions (WT, R153C, and R114C) were synthesized individually by Synbio Technologies as XhoI/HpaI fragments (of 2270bp) and cloned into the XhoI/SnaBI site of the pBMN-I-Hygro vector. The three sequences were confirmed by Sanger sequencing.

Immortalized melan-b melanocytes derived from mice homozygous for the *TYRP1*^b allele were cultured as described.^{53,54} Melan-b cells were infected with recombinant retroviruses encoding *TYRP1* variants (described above). Briefly, Plat-E cells⁵⁵ were cultured and transfected with the retroviral vectors described above, empty pBMN-I-hygro, or pBMN-I-hygro expressing mCherry-tagged human STX13⁵⁶ using Lipofectamine 2000. The medium was replaced with fresh melanocyte medium the following day and cell supernatants were harvested 48–72 h post-transfection as described.⁵⁷ The medium, containing recombinant retroviruses, was used directly to infect melan-b cells as described⁵⁸ except that cells were seeded the previous day in a 10-cm dish. Two days later the medium was supplemented with 500 mg ml⁻¹ hygromycin B to select for infected cells. Antibiotic-resistant cells were used directly as polyclonal cell populations for experiments. Two separate stable lines per construct were selected and included in the analyses.

We performed spectrophotometric assays or melanin and protein content as described.^{58,59} Briefly, melanocytes in a confluent 10-cm dish were harvested by trypsinization. Cells were counted, and duplicate samples of 10⁶ cells for each experimental condition per experiment were washed once with RPMI + 10% FBS and twice with ice-cold PBS, and then resuspended in 50 mM Tris-HCl, pH 7.4, 2 mM EDTA, 150 mM NaCl, 1 mM dithiothreitol, and cOmplete Protease Inhibitor Cocktail Tablets (Roche). Cells were probe-sonicated on ice using the Sonic Dismembrator Model 100 (Fisher Scientific), and sonicates were fractionated into supernatant and pellet fractions by centrifugation at 20,000 x g for 15 min at 4°C. Protein concentrations in supernatants were estimated using the DC

colorimetric protein assay (Pierce) with a standard curve derived using differing concentrations of BSA. Melanin-containing pellets were washed in 500 μ l 50% ethanol, 50% ether, collected by centrifugation at 20,000 \times g, and resuspended in 1 ml of 2 M NaOH, 20% DMSO. Melanin was solubilized by heating at 60°C for 40–60 min and quantified using spectrophotometry to measure Optical Density (OD) at 492 nm. OD values were normalized to total protein content in each lysate. The assay was performed on six different days using samples collected from two different sets of stable cell lines per construct.

We performed imaging and analysis as described.⁵⁶ Briefly, melanocytes were seeded onto Matrigel-(Corning) coated coverslips 48–72 h before fixation. Cells were fixed with 2% formaldehyde in PBS for 20 min, washed briefly with PBS, then labeled with TA99/Mel-5 antibody to TYRP1 (American Type Culture Collection, Rockville, MD) diluted in blocking buffer (PBS, 0.1% BSA, 0.02% saponin) for 1 h at room temperature (RT). After a 15-min wash in PBS, cells were incubated with Alexafluor 488-labeled donkey anti-mouse IgG (Jackson ImmunoResearch) diluted in blocking buffer for 30 min at RT. Samples were washed for 15 min in PBS, mounted with Prolong Gold Antifade Mountant (Invitrogen), and analyzed by epifluorescence microscopy on a DMI 6000B microscope (Leica Biosystems) equipped with a 63x plan apochromat (Plan Apo) objective (1.4NA) and a Hamamatsu Photonics ORCA-Flash4.0 sCMOS digital camera. Both fluorescence and bright field images were acquired as a z-series with 0.19- μ m steps and were deconvolved using the blind deconvolution algorithm of Microvolution software (Bio-Vision Technologies) and ImageJ. Final images were composed using Adobe Photoshop software.⁵⁸ Images were quantified using ImageJ.

To quantify the percentages of cells with varying levels of pigmentation, bright field images of individual cells within randomly chosen fields were characterized as non-pigmented (no visual pigmentation or fewer than 10 pigment granules per cell), densely pigmented (easily visualized pigmentation throughout the cell with numerous granules), lightly pigmented (signal above background but either very low signal or fewer than 40% of the total number of granules for wild-type cells), or lightly pigmented with prominent pigment aggregates (structures larger than 1 micron in diameter, typically one or two per cell). Data from three experiments with 200 cells per sample type per experiment were analyzed by mixed effect analysis and Tukey’s multiple comparison test.

To quantify the TYRP1 staining pattern, cells in randomly chosen fields were characterized as having predominantly ring-like structures (easily detectable “donuts” of less than 1 micron in diameter), diffuse and/or punctate staining (hazy cytoplasmic fluorescence and/or small puncta with no visible lumen), or a combination of both. Cells were analyzed blinded and without observing pigmentation status. Data from four experiments with 150 cells per sample type per experiment were analyzed by two-way ANOVA (because there were multiple variables) with Dunnett’s multiple comparison test.

The area of overlap between TYRP1 and pigmented melanosomes in the cell periphery of melanocytes was quantified using a thresholding approach in ImageJ on deconvolved fluorescence images as detailed.⁵⁶ Briefly, images were cropped to individual representative cells that had sufficient pigmentation to allow for thresholding. Both the bright field image and the corresponding deconvolved TYRP1 immunofluorescence image were subjected to the following manipulations. Background was subtracted using the Background Subtract function with a rolling ball radius of 2 microns, and then an identical mask corresponding to the perinuclear region (which is typically very densely labeled by TYRP1) was cropped out of both images. The Adjust>Threshold function was used to generate binary images that closely resembled the original images. Structures larger than five pixels were quantified using the Analyze Particles function, the area of overlap between the two images was calculated by using the Math>Multiply function, and values were calculated relative to the total area of thresholded bright field objects. Data from at least 30 cells of each cell type from three independent experiments were analyzed by Kruskal-Wallis test (because the data were not Gaussian) with Dunn’s multiple comparison test.

All statistical analyses were performed using Graphpad Prism 9 for MacOS.

Allele age

We estimated the age of *TYRP1*^{R153C} using *runtc*,²⁶ a program that estimates the time of first coalescence to the nearest variant on a chromosome. To increase sample size for this analysis, we used the combined high and imputed low coverage data for HiC_scaffold_24. We reran the GLIMPSE pipeline on the low coverage samples where the high coverage reference panel was not first filtered for MAF, thereby leaving more singletons in the reference dataset for coalescence with the focal allele. We estimated the coalescence time for all variants on the scaffold with all range wide samples together, as well as separately in the western lineage, Southeast Alaska (SEAK), and eastern populations separately, using a mutation rate of 1×10^{-8} and the recombination rate from the dog genome, 0.97cM Mb⁻¹. We report all and lineage specific distributions and variant estimates in [Figure S3A](#).

Demography

We inferred the demographic history of *U. americanus*, then tested if spatial patterns of *TYRP1*^{R153C} alleles were due to neutral or adaptive processes given the demography. We first assessed *U. americanus* population structure using PCA. We aligned a previously generated RAD-Seq dataset⁷ to the *U. americanus* reference genome and called SNPs using STACKS v2.53,⁶⁰ including filters for one SNP per RAD-tag, >80% genotyping success per locus, and MAF > 0.05; this resulted in 37,422 SNPs. We pulled down those loci from the high coverage WGS samples to increase the sample size (n = 117). We ran a PCA analyses in PLINK v1.9^{61,62} using the RAD-seq+hcWGS and observed a concordant pattern to the previous analysis⁷; thus, we felt confident with analyzing lineages and populations as previously determined.

We estimated change in effective population size (N_e) through time using MSMC2.⁶⁹ For this analysis we used scaffolds 2–37, and made individual mask files with the bamCaller.py script, then used the phased datasets to make genome-wide masks with SNPable.⁷⁰ We generated input scripts using generate_multihetsep.py. Output was converted to years and number of individuals using a mutation

rate of 1×10^{-871} and a generation time of 6.5 years.⁷² We ran MSMC2 on three samples (six haplotypes) from both the eastern and western lineages, and the admixed SEAK population. Historic N_e was approximately 30,000. From 100–10kya N_e declined to 3,000 in the western lineage, yet remained constant in the eastern lineage. N_e also declined in Alaska from 50–10kya to approximately 8,000. MSMC2 plots indicate N_e increased since the Last Glacial Maximum (18–22kya). This demographic history provides an explanation for the low haplotypic diversity in Nevada as the ancestral and causative alleles sit on highly homogeneous haplotypes (Figures S1 and S4). Using the output from MSMC2, we further estimated the cross-coalescent model and input results into MSMC-IM²⁷ to estimate the patterns and timing of population divergence (using MSMC2 estimates), and rate of gene flow over time (using PSMC' estimates on two haplotypes for the Idaho and Arizona samples). Estimates may be inaccurate in the most recent time lags of MSMC2 analyses warranting caution when estimating contemporary N_e . Our data appear to have a limit for inferences younger than 1–5kya.

While our demographic model infers broad patterns of lineage relatedness, it does not identify the directionality of range expansion; thus, we used the RAD-seq+hcWGS dataset to understand patterns of range expansion via the directionality index (Ψ).⁷³ We removed geographic sites with fewer than three samples for a total of 111 samples across 23 populations. We input genotypes and geographic data into the *rangeExpansion* package in R, then calculated Ψ for all population pairs using the *get.all.psi* function. We determined the significance of each pairwise Ψ estimate by calculating the standard error of the upper triangle of the matrix excluding the diagonal, then calculating a Z-score for each pairwise comparison. To visualize the range expansion patterns, we plotted pairwise values where $Z > |5|$ within the western and eastern lineages, and between the two lineages and SEAK (Figures S3B–S3D).

Selection tests

We calculated π (π) using VCFTOOLS⁷⁴ in 1kb sliding windows with a 100bp step size from the imputed low coverage WGS data using samples from the Nevada (western lineage; $n = 38$), SEAK ($n = 95$), and Appalachian Mountains (representative of eastern lineage; $n = 38$) populations. We further calculated F_{ST} between black and brown animals within either the Nevada or SEAK populations using the same sliding window scheme.

We tested for a selective sweep surrounding *TYRP1* using both integrated haplotype score (iHS) and extended haplotype homozygosity (EHH)⁷⁵ implemented in *selscan* v2.^{76,77} The iHS analysis was run on scaffold 24 of the *U. americanus* reference genome within the Nevada population, then normalized based on allele frequency using the *norm* function within *selscan* v2. No sites within the haplotype block carrying *TYRP1*^{R153C} had iHS scores greater than |2|. We ran the EHH analysis in both the Nevada and SEAK populations using the *-keep-low-freq* flag. Further, we identified 15 sites on each of the 36 long scaffolds (or 540 sites each) that matched the derived allele frequency of R153C within each test population and ran EHH on each of those sites. We compared the decay curves of R153C to these allele frequency matched background loci as a test if the decay in haplotype homozygosity was within the range of the background (Figure S5). While decay curves between the ancestral and derived alleles suggested extended haplotype homozygosity for the derived R153C, the background matched samples showed the overall scores were not out of range for the background sites. Both the low N_e within the Nevada population and low selection coefficient complicate the analysis of selection, as simulation studies suggest low power to detect selection under these conditions.⁷⁸ Moreover, we chose not to use cross-population sweep tests due to the decrease in power with increasing divergence, and our estimates that the eastern and western lineage populations diverged $\sim 15.8k$ generations ago.⁷⁶

We further tested for possible drivers of selection using BayEnv2.^{30,79} Using the combined RAD-Seq, hcWGS, and lcWGS data at the RAD loci, we clustered the data into 24 geographic areas, identified a centroid longitude and latitude coordinate, then extracted values of 11 climate variables and altitude for each coordinate. The climate variables from the CliMond dataset^{80,81} included: bio1 (annual mean temperature), bio3 (isothermality), bio4 (temperature seasonality), bio5 (max temperature of warmest week), bio6 (min temperature of coldest week), bio10 (mean temperature of warmest quarter), bio11 (mean temperature of coldest quarter), bio12 (annual precipitation), bio19 (precipitation of coldest quarter), and bio20 (annual mean radiation). Beyond the climate variables, altitude, latitude, and longitude were all tested as selective forces. Finally, we used the presence or absence of *U. arctos* on the landscape as a factor. For each geographic location, we scored the site with the presence of *U. arctos* before range contraction due to human activity based on maps of the expected species distribution.⁸² We prepared the covariance matrix using PGDSpider,⁸³ and the environmental matrix according to the BayEnv2 manual. We ran 100,000 iterations of the model and analyzed the Bayes Factors (Table S4) for the alternative hypothesis that the variable of interest was a selective force on allele frequency of *TYRP1*^{R153C}.

Gene flow simulation

To test if a model of gene flow without selection could produce the spatial gradient of declining frequency of the alternative allele along a south-to-north axis in the western range, we used the forward genetic simulation program SLIM3.⁸⁴ We modeled four populations, broadly representative of Nevada, Arizona/New Mexico, Idaho, and SEAK. These population were selected as we have at least one high coverage genome from each population (key resources table). We reran MSMC-IM on one genome from each population for all pairwise combinations to estimate historic gene flow rates to use as input in our model (Figure S6).

Our model seeds a new variant (i.e., R153C) at a frequency of 1% into the Nevada population at generation 0, then tracks allele frequency within each population for 1,440 generations such that we get a simulated estimate to compare to observed data. Our data suggests that R153C has a dominance coefficient (h) greater than 0.5, but not 1; thus, we varied h from 0 to 1 using 0.1 increments. Further, we ran each model with a selection coefficient (s) of either 0, 0.005, or 0.01. MSMC-IM estimates bidirectional gene flow, thus for each population pair we use the peak estimated rate (Figure S6) since the Last Glacial Maximum (LGM). We ran three

different models varying the selection coefficients ($s = 0, 0.005, \text{ or } 0.01$). From generations 980–1,310, population size increased in each population at a per generation rate of 10^{-6} which was a rate approximated from our MSMC results. At generation 1,390 (i.e., 50 generations prior to the end of the simulation and meant to represent anthropogenic influences on bear populations), we imposed population specific bottlenecks given estimates from the literature. Specifically, the Nevada population was reduced to 100,⁸⁵ and the Arizona/New Mexico, Idaho, and SEAK populations were reduced to 5,000, 7,000, and 4,000 respectively.⁷ We ran 1,000 iterations of each model. We recorded the number of simulations in which the derived allele went extinct in all populations or was still polymorphic following 1,440 generations (no simulations observed the derived allele fixing in all populations; reported in the legend of [Figure 6](#)). For simulations where the locus remained polymorphic, we averaged the frequency within each population across simulations, and compared to the observed frequency from our qPCR assay and contour plots of percent of black animals in the population.

This simulation with 33 different scenarios (h by s combinations) identified that both increasing values of h or s resulted in increased allele frequencies and decreased probability of allele extirpation from the landscape. We reran the simulation with an h of 0.75 for the final model ([Figure 6](#)).